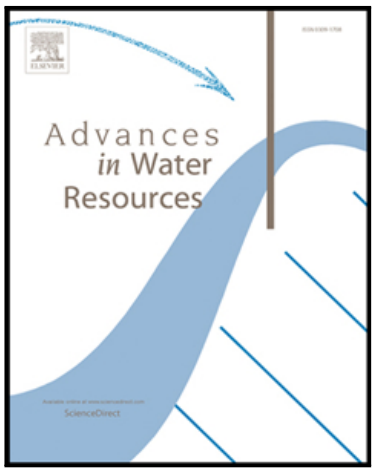

A Fully 3-D Numerical Model to Predict Flood Wave Propagation and Assess Efficiency of Flood Protection Measures

Daniel Horna Munoz , George Constantinescu

PII: S0309-1708(17)31142-9
DOI: https://doi.org/10.1016/j.advwatres.2018.10.014
Reference: ADWR 3222

To appear in: *Advances in Water Resources*

Received date: 7 December 2017
Revised date: 12 October 2018
Accepted date: 15 October 2018

Please cite this article as: Daniel Horna Munoz , George Constantinescu , A Fully 3-D Numerical Model to Predict Flood Wave Propagation and Assess Efficiency of Flood Protection Measures, *Advances in Water Resources* (2018), doi: https://doi.org/10.1016/j.advwatres.2018.10.014

HIGHLIGHTS

- 3D models can be used to accurately predict flood wave propagation in natural environments
- 3D non-hydrostatic models can be used to study cases when flow becomes locally pressurized
- 3D models can be used to estimate effectiveness of flood protection measures

A FULLY 3-D NUMERICAL MODEL TO PREDICT FLOOD WAVE PROPAGATION AND ASSESS EFFICIENCY OF FLOOD PROTECTION MEASURES

Daniel Horna Munoz[1,2] and George Constantinescu[1]

[1]Department of Civil and Environmental Engineering and IIHR-Hydroscience and Engineering, The University of Iowa, IA 52242, USA

[2]Department of Environmental Engineering and Centro de Investigación y Tecnología del Agua (CITA), Universidad de Ingeniería y Tecnología (UTEC), Barranco, Lima, Peru

KEYWORDS: Floods, Numerical Simulations, Flood mitigation

Abstract

This paper discusses development and validation of a 3-D, non-hydrostatic, Reynolds-Averaged Navier-Stokes (RANS) model using the Volume of Fluid (VOF) approach to simulate flooding events in natural environments. A series of validation simulations in simple and complex geometries are performed to test the different modules of the flow solver. The paper also discusses the differences between simulation results obtained using the 3-D model and those obtained using a standard, 2-D hydrostatic, depth-averaged model. The predictions by the two models show fairly large differences in regions where 3-D effects are expected to be significant (e.g., in regions containing highly-curved river reaches and near hydraulic structures). Then, the validated 3-D model is employed to investigate the efficiency of using flood-protection walls to reduce adverse effects of flooding in the Iowa River near Iowa City, Iowa, USA. Finally, the propagation of a flood wave in a reach of the Iowa River containing a bridge is simulated and the effects of the flow becoming pressurized beneath the bridge deck are discussed. For such applications, in which the regime can change locally between open channel and pressurized flow, the use of fully 3-D, non-hydrostatic models may be the only viable option to accurately predict flow hydrodynamics and its effects on bed shear stresses and sediment entrainment potential, especially around locations where the flow becomes pressurized.

1. Introduction

Several studies have shown that the frequency of flooding will increase under current changing climatic conditions (Milly et al. 2002) making flooding a crucial topic of research for future planning of cities and major industrial works (Mossa, 2007). Flooding can have great repercussions on urban environments and can damage almost all structures placed over the floodplain (Molinari et al., 2017). Being able to predict the flood extent and flood wave propagation is of great importance for hydrologists and urban planners. The proliferation of high-resolution digital elevation maps, hydrographic data and rapid development of efficient numerical tools has resulted in the development of hydrodynamic models capable of producing quantitative assessments of flood risk at very fine spatial and temporal scales (Hunter et al. 2007). Numerical models can also play an important role in the management of flood hazard and in investigating the efficiency of different flood protection measures (Radice et al., 2012).

Flooding in riverine environments is a very complex hydrodynamic phenomenon, in particular because of the flow interaction between the channel and its floodplain, strong curvature effects and because of complex river dynamics in cases when the river contains man-made hydraulic structures. As a result, 3-D effects may be significant in many practical applications involving flood-wave propagation, at least over certain regions and at certain times, and affect capacity of numerical models to accurately predict flood extent, peak flood levels and time to peak.

Information on flood extent and flood wave propagation is usually obtained from 1-D (e.g., Bates and Roo, 2000; Omer et al., 2003; Casas et al., 2006; Mohamed et al., 2006) and 2-D (e.g., Wagner and Mueller, 2001; Dhondia and Stelling, 2002; Musser and Dryer, 2005)

models that solve the St. Venant (shallow water flow) equations with bed roughness parametrization based either on Chezy or Manning's coefficient. Another popular approach is based on the use of hybrid 1-D/2-D models in which the 1-D equations are solved along the main streams and the 2-D equations are solved over the floodplains (Frank et al., 2001; Dhondia and Stelling, 2002). These models are subject to limitations associated with simplifications and assumptions inherent to depth averaging or section averaging the governing equations of motion. For instance, even 1-D models that solve the dynamic wave equation (e.g., HEC-RAS, MIKE11) cannot accurately simulate lateral flow into the floodplain, whereas 2-D hydrostatic models cannot accurately predict flow in regions (e.g., around areas of high channel curvature, bridge piers, groynes, large bottom depressions, submerged islands) where separation and strong adverse pressure gradients are present (Frank et al., 2001; Haque et al., 2007). Overall, standard hydrostatic 1-D and 2-D models were shown to be successful in some cases, but also to sometimes provide inaccurate predictions of the flood depth, flooded area and flood-wave propagation speed during the flood event (see Concerted Action on Dam-Break Modeling Final Report, 2000). Consequently, most often, large safety factors have to be added when results of these simulations are used to develop strategies to mitigate adverse flood effects.

To alleviate some of these deficiencies and limitations of standard lower-order models, more advanced, non-linear versions of 2-D models were proposed to account for 3-D secondary cross-stream motions induced by curvature effects (e.g., Vasquez et al., 2011; Gamry and Steffler, 2005; Blanckaert and de Vriend, 2010; Ottewanger, 2013) and for non-hydrostatic effects over irregular topography (Bristeau et al., 2011; Lu et al., 2015; Arico et al., 2016). Both types of corrections use additional modeling assumptions to approximatively account for 3-D effects. For example, all up-to-date non-hydrostatic 2-D model corrections assume a

linear distribution of the dynamic pressure and vertical velocity over the flow depth. Obviously, the assumption of vertical velocity linear variation over the flow depth is violated in regions where secondary flow motions are strong and contain multiple cells or if motions near the free surface are violent (Lu et al., 2015). Still, such models were found to accurately predict free surface dynamics in complex cases involving: 1) wave propagation over a deformed bed containing a submerged or an emerged flow obstruction; and 2) wave propagation associated with a dam-break or solitary waves/tsunamis (Arico et al., 2016). In principle, more complex assumptions are possible (e.g., use of multiple layers in the vertical direction over which a linear profile with different slopes in each layer may be assumed) that should further improve simulation of dispersive effects (e.g., accurately capturing wave phase) in such models (see discussion in Lu et al., 2015; Arico et al., 2016). Such models have yet to be proposed and tested. In this regards, data from 3-D non-hydrostatic simulations can be depth averaged and used to test the performance of these corrections, as well as that of the simplifying assumptions and modeling of different terms in the governing equations of these lower-order models. To our knowledge, none of the afore-mentioned non-hydrostatic 2-D models were used to predict flood wave propagation over natural terrain containing one or multiple streams together with their floodplains and man-made structures (e.g., buildings, hydraulic structures), which is the main type of application of interest for the present study. More importantly, this type of non-hydrostatic corrections for 2-D models cannot be applied for cases where the flow can locally change regime from open channel to pressurized, a situation often encountered in real applications in which bridges, culverts and other hydraulic structures are present over the flooded region.

Another important point is that all types of 1-D and 2-D models require extensive calibration for different flow conditions. 3-D models that use meshes that are fine enough to insure a

grid-independent solution and resolve the large-scale topography features and the other structures present over the deformed terrain require much less calibration. On the other hand, the main advantage of 1-D and 2-D models is that they can be applied to predict flood propagation over relatively large domains (e.g., tens of kilometers in each horizontal direction) and over large periods of time (e.g., flood hydrographs with a duration of months), something that is not yet possible using fully 3-D models because of the high computational resources needed both in terms of physical time to obtain the solutions and in terms of data storage and data postprocessing.

A way to overcome the limitations of 2-D models to accurately predict flood wave propagation over natural terrain containing large-scale man-made structures (complex domains) that introduce strong non-hydrostatic effects is the use of fully 3-D, non-hydrostatic models with free-surface tracking capabilities. Ideally, Large Eddy Simulation (LES) techniques should be used for such simulations (Rodi, Constantinescu and Stoesser, 2013; Khosronejad et al., 2016), but this approach will remain computationally too expensive for applications involving flood wave propagation over naturally deformed terrain for at least 1-2 decades. However, for steady flow conditions, state-of-the-art 3-D, non-hydrostatic, RANS models can predict mean flow hydrodynamics in channels with natural bathymetry with an accuracy that is comparable to that of LES (Zeng et al., 2008a, 2010; Keylock et al., 2012) and 3-D unsteady RANS is feasible for applications involving flood wave propagation, at least for relatively short flood events.

The flow field increases its level of three dimensionality (e.g., stronger vertical accelerations, changes in the dominant flow orientation with the distance from the bed, flow separation in vertical planes, secondary cross-flow motions) during unsteady events such as floods. This is

why careful validation is needed before applying such 3-D models to highly unsteady problems over complex topography. The availability of the 3-D flow fields allows a better understanding of the flow physics during the flood-wave propagation and, in particular, how secondary flow develops in time, how the flows over the floodplain and the deeper parts of the main channel interact, how the streamwise momentum is redistributed and how the potential for sediment erosion changes during the flood event. Finally, there is an important class on engineering applications in which the flow regime can change locally from open channel flow to pressurized flow. Example of such applications are flood wave propagation in domains containing culverts and bridges where accurate estimation of the interaction of the flow with the hydraulic structure, prediction of bed shear stresses and pressure scour effects cannot be obtained even with state-of-the-art 2-D models (Frank et al., 2001). For such applications, the use of 3-D non-hydrostatic models is basically the only option to obtain accurate solutions.

Though the use of 3-D, non-hydrostatic, RANS models with advanced turbulence models (e.g., k–ε, k–ω, SST) in hydraulics and river engineering has become very popular (Rodi, 1984; Olsen and Stokseth, 2010), their application to simulate flooding problems has been very scarce and mainly focused on dam-break problems (Biscarini et al., 2010, 2016; Yang et al., 2010). For example, Biscarini et al. (2010) found that predictions obtained using a 3-D model developed in OpenFoam were overall more accurate than those obtained using a state-of-the-art 2-D model (CCHE-2D) for several dam-break test cases for which validation data were available form laboratory experiments (Soares-Frazao, 2002; Soares-Frazao and Zech, 2002). The development of such 3-D models requires careful validation. This is especially important for the deformable free surface module, which is essential to any simulations involving the propagation of a flood wave. Though different methods can be used to track the

free surface, all methods are subject to errors and their performance for flooding problems is not clear. Another big challenge is to determine the minimum level of grid refinement needed to obtain accurate predictions of flood evolution in time. The required level of mesh refinement is different in different parts of the domains. Using very fine meshes over the whole computational domain is not an option, given the huge computational costs required to simulate flood propagation in 3-D even for relatively small regions.

The present paper describes the main features of a fully 3-D, non-hydrostatic, RANS model to predict flood propagation in natural domains. The model uses the Volume of Fluid (VOF) method to account for free-surface deformations. Following validation for relevant simpler cases, the capabilities of the model to predict flood wave propagation over natural bathymetry containing various types of large-scale structures are illustrated for several important types of applications including for a case when the flow becomes pressurized over a limited region during high-flow conditions.

2. Numerical Model

The engine of the present 3-D model to simulate flood wave propagation in complex domains is the pressure-Poisson solver in STAR-CCM+. The governing equations solved in the RANS approach are the continuity and momentum equations:

$$\frac{\partial U_i}{\partial x_i} = 0 \tag{1}$$

$$\frac{\partial U_i}{\partial t} + \frac{\partial (U_i U_k)}{\partial x_k} = -\frac{1}{\rho}\frac{\partial}{\partial x_k}\left[(\mu + \mu_t)\left(\frac{\partial U_i}{\partial x_k} + \frac{\partial U_k}{\partial x_i}\right)\right] - g\delta_{i3} \tag{2}$$

where U_i is the velocity component along the i direction, ρ is the density of the fluid, μ is the molecular dynamic viscosity, μ_t is the eddy viscosity predicted by the RANS model, P is the pressure, g is the gravity and i=3 corresponds to the vertical direction. The realizable

k–ε turbulence model using the two-layer formulation is used to calculate μ_t. The transport equations for the turbulent kinetic energy, k, and the turbulent dissipation rate, ε, are:

$$\frac{\partial k}{\partial t} + \frac{\partial (kU_j)}{\partial x_j} = -\frac{1}{\rho}\frac{\partial}{\partial x_j}\left[\left(\mu + \frac{\mu_t}{\sigma_k}\right)\left(\frac{\partial k}{\partial x_j}\right)\right] + \frac{f_c G_k}{\rho} - \varepsilon \quad (3)$$

$$\frac{\partial \varepsilon}{\partial t} + \frac{\partial (\varepsilon U_j)}{\partial x_j} = -\frac{1}{\rho}\frac{\partial}{\partial x_j}\left[\left(\mu + \frac{\mu_t}{\sigma_\varepsilon}\right)\left(\frac{\partial \varepsilon}{\partial x_j}\right)\right] + \frac{f_c C_{\varepsilon 1} S\varepsilon}{\rho} - \frac{\varepsilon}{k+\sqrt{\mu\varepsilon/\rho}} C_{\varepsilon 2}\varepsilon \quad (4)$$

The eddy viscosity is then calculated as:

$$\mu_t = \rho C_\mu \frac{k^2}{\varepsilon} \quad (5)$$

where f_c is a curvature correction factor, G_k is the production of turbulent kinetic energy due to velocity gradients and C_μ rather than being a constant, as is the case in the standard k-ε model, is a function of the mean rate of strain tensor magnitude, mean rate of rotation tensor magnitude, k and ε. The exact expression of these terms along with the values of the other model constants in equations (3), (4) and (5) can be found in Wilcox (1998). The two-layer approach allows the standard realizable $k-\varepsilon$ turbulence model to be applied inside the viscous sublayer if the mesh is fine enough to resolve this layer by dividing the computational domain into two regions: one close to the wall and one away from it. In the layer close to the wall, ε and μ_t are defined as functions of the wall distance. The values of ε obtained in the near wall layer are then blended smoothly with the values obtained in the outer region where equation (4) is solved. The transport equation for k is solved everywhere in the domain. Details on the two-layer k-ε model can also be found in Wilcox (1998). This version of the k-ε model was shown to perform well compared to other state-of-the-art RANS models for complex turbulent flows (Constantinescu and Patel, 2000; Kashyap et al., 2012). The Volume-of-Fluid (VOF) method is used to track the location of the deformable free surface. A layer of air is present over the parts of the domain that contain, or can contain, water during the simulation. The VOF method is based on the advection of the volume

fraction of water, α, for which a standard advection equation ($\frac{\partial \alpha}{\partial t} + U_j \frac{\partial \alpha}{\partial x_j} = 0$) is solved. In cells fully occupied by water α=1, while in cells containing only air α=0.

The finite-volume Navier-Stokes code solves equations (1) and (2) integrated over elementary control volumes. The advective terms are discretised using a second-order accurate upwind scheme, while the discretization of the transient (unsteady) term is second-order accurate in time based on an implicit representation. The diffusive and pressure gradient terms are discretised using the second-order, central-differences scheme. The SIMPLE algorithm is used for solving the discretised Navier-Stokes equations. In the SIMPLE algorithm, an intermediate velocity is obtained by solving the momentum equations without the pressure gradient term. The intermediate velocity field does not satisfy the continuity. A pressure correction algorithm is employed to modify the pressure field and in turn modify the mass fluxes and velocity fields such that the corrected velocity field satisfies continuity. Equations (3) and (4) are integrated in a similar way to the momentum equations, but the first-order upwind scheme is used to discretize the convective terms. The temporal discretization is second-order accurate in time. The Navier-Stokes solver was already successfully used to predict steady flow in complex domains (Basnet et al., 2015; Cheng et al., 2017). The advection term in the VOF equation is discretised using the second-order upwind scheme. The temporal discretization is second order accurate. Though the VOF module of the code was validated for many applications, predicting flood events requires additional validation given that the flow is very shallow over large parts of the domain and rapid changes in the free surface can occur in regions where hydraulic structures are present. The viscous solver in STARCCM+ is parallelized using MPI and has shown good scalability on PC clusters up to 1,000 processors.

Mesh generation is a critical step in being able to perform accurate simulations of flood events in complex and large domains in a reasonable amount of time. STAR-CCM+ contains a very powerful meshing capability in which an initial surface geometry (e.g., topography of the terrain) can be imported, then smoothed in such a way to improve computational efficiency (use of relatively large time steps) without any significant loss of resolution of the main terrain features. For applications in natural environments containing river reaches, the level of refinement decreases as one goes from regions situated close to hydraulic structures to the river channel and then to the floodplains and outer regions (e.g., regions containing air away from the water-air interface). This is an important step, since a surface mesh of the boundaries is needed before creating a volume mesh.

Once the geometry has been processed, a volume mesh is created. The goal is to obtain a high quality mesh with a sufficient level of grid refinement in critical regions of the flow. Mesh topologies include tetrahedral, hexahedral and polyhedral models with mesh refinement near the boundaries. In the present simulations, hexahedral meshes were generally chosen, since the control over the size and number of cells becomes more intuitive and because the discretization errors are generally smaller for such meshes. Hexahedral meshes are created using a meshing module that generates cube-like cells based on the specified cell size on the surface (boundary) mesh. It is also possible to create cells with different edge sizes in each direction. This feature makes the use of this meshing module highly suitable for domains containing river channels and their floodplains, since the mesh can be refined in the vertical direction while maintaining relatively large edge sizes in the horizontal directions. The anisotropic cells are created in the pre-specified sub-regions during the surface re-meshing procedure, making the surface mesh consistent with the volume mesh. For applications in natural environments, the horizontal mesh resolution near hydraulic structures is between

one-half to one-fourth of the horizontal mesh resolution in the river channel, while the horizontal mesh resolution over the floodplains is twice that of the river channel. The vertical mesh resolution in the three previously-mentioned regions is about the same. The vertical mesh resolution in the regions containing air away from the water-air interface is about one order of magnitude larger than the mesh size in the river channel. Additional mesh refinement is generally performed near solid boundaries by creating high-aspect ratio, highly-skewed cells named prism layers parallel to the boundary's surface. Generally the size of the first prism layer is chosen to be close to 100 wall units in the wall normal direction, unless an equivalent roughness height is specified. In the latter case, the desired wall spacing is equal to twice the roughness height. Local roughness elements larger than 3 cm are resolved by the mesh in the applications discussed in the present paper.

The outlet and top (opened to air) boundaries where specified as pressure outlets. The desired pressure and volume fraction of water were directly specified on all outlet and top boundary surfaces. Specifying the distribution of the volume fraction of water is equivalent to imposing a free surface elevation at the outlet boundary. In the case when air is present next to the outlet boundary or the top boundary, the pressure outlet boundary was 0 Pa and the volume fraction of water was set to $\alpha=0$. The inlet was specified as a velocity inlet with a specified level of the free-surface. No-slip (zero velocity) boundary conditions were specified at the walls (channel surface, floodplain and surfaces of hydraulic structures). In some simulations of laboratory experiments the terrain boundaries were assumed to be smooth. For applications in natural environments, the terrain boundaries were assumed to be rough. The roughness height was set to two times the median grain size in the corresponding main channel or floodplain region of the topography.

The 2-D simulations were performed using the SRH-2D code (Lai, 2008, 2010), which solves the full St.-Venant equations with a parabolic turbulence model. Roughness parametrization is accounted for by specifying different values for the Manning's coefficient over the various parts of the topography. All 2-D simulations in complex domains were performed with calibrated values of the Manning coefficient determined for the Iowa River reach.

3. MODEL VALIDATION

3.1. Flow in an S-shaped open channel

This subsection compares the numerical solution with experimental data for steady flow in an open channel (Figs. 1 and 2) which was investigated in the lab by Yen (1967). The S-shaped channel contains two identical 90° bends connected by a small straight reach (Fig. 1). The channel has a trapezoidal cross sectional geometry with 1:1 side slopes. The bottom width is B_b=1.83 m. The radius of curvature of each bend is 8.54 m. The mean inlet velocity is U=0.692 m/s and the water depth at the inlet is H=0.156 m. Using these variables, the channel Reynolds number is close to 10^5 and the Froude number is equal to 0.6. The computational mesh contains 550,000 cells with a near-wall refinement equivalent to 2.5 wall units.

Figure 2 shows the measured and computed non-dimensional streamwise velocity profiles over the depth at Section S0 (Fig. 1). Results are plotted at five different locations along the transverse direction (η/B), where η is measured from the center of the channel. The largest differences between numerical predictions and the lab-measured velocity profile is observed at η/B=-0.461 where the simulation underpredicts the measured velocity at all flow depths. At the other locations, the simulation results show good agreement with the experimental data.

Figures 3 and 4 show the transverse free-surface profiles at four cross sections and the longitudinal free-surface profiles along the two banks of the channel, respectively. The free surface corresponds to the α=0.5 iso-surface. The transverse free-surface profiles predicted by the simulation are in good agreement with experimental data at all the four cross-sections shown in Fig. 3. In Fig. 4, a positive free-surface deflection is observed at the outer bank while a negative deflection is observed at the inner bank. This behavior is induced by centrifugal force effects induced by channel curvature. The computed longitudinal free-surface profiles show the same trend as the measured data. A slight over prediction of the free surface elevation is observed at the outer bank and a slight under prediction is observed at the inner bank based on the longitudinal free-surface deflection. The observed level of agreement between the present 3-D simulation and the experimental data is comparable to the one observed for other 3-D RANS models (Zeng et al., 2008b). The good agreement observed between predictions and measurements of the velocity and free surface profiles for this test case prove that the present numerical model is capable of accurately simulating open channel flow problems where curvature effects and the associated cross-stream secondary flow are controlling the free surface deformations.

3.2. Dam break in a straight open channel

In the hypothetical abrupt failure of a dam bordering a reservoir, the blocked column of still water spreads suddenly into the adjacent region downstream of the reservoir. The most idealized case that mimics such an event is the one in which a rectangular column of water collapses on a flat horizontal surface. Martin and Moyce (1952) studied this problem experimentally by collapsing a square column of water of height a = 5.7 cm into an 28.5 cm long by 7.2 cm high channel of rectangular cross section. The parameters tracked during the

experiment were the front surge position measured from the left wall, *x*, and the remaining water column height at the left wall, η.

The length and height of the computational domain size were 5a and 1.25a, respectively, consistent with the computational domain employed by Kelecy and Pletcher (1997) and with the experiment. The left, right and bottom boundaries were no-slip smooth walls. A pressure outlet boundary condition was specified at the top boundary. Figure 5a shows the general layout of the 2-D dam break test case. Results are presented for a simulation performed using 800x200 mesh points in the horizontal and vertical directions, respectively. The solution on this mesh was checked to be grid independent and also to conserve the total volume of water with an error of less than 2% during the duration of the simulation.

Figures 5b and 5c show that the simulation accurately predicts the temporal evolution of the front position and the remaining water column height as a function of the non-dimensional time, t/T_0, where the time scale is $T_0=a/(ga)^{1/2}$ and g is the gravitational acceleration. This is a very relevant test case for applications in which the hydrograph describing the flooding event is characterized by large and rapid variations in the stage.

4. Flood wave propagation in a domain containing an 18-km long reach of the Iowa River

This sections tests the model capabilities to simulate steady flow and a flood wave propagating in a reach of the Iowa River containing hydraulic structures. Figure 6 shows the location and horizontal extent of the computational domain. The computational domain starts right downstream of the flood control dam (Section 1-1) where a river gaging station is present (Section 1'-1'). The end of the computational domain is located some distance

downstream of the second river dam (Section 2'-2'), which is close to Iowa City, USA. Both river dams are in fact weir-like structures. The arrow points at Clear Creek, the main tributary feeding into the Iowa River near Iowa City. The inclusion of Clear Creek is of great importance due to significant backwater effects from the Iowa River into Clear Creek during high flow conditions. A second river gaging station is situated approximately 100 m downstream of the second river dam (Section 4-4). The bathymetry/topography information is also shown in Fig. 6. The bathymetry was collected using single- and multi-beam hydrographic surveys while the topography information was obtained from 1 m resolution LiDAR data. Also included are the locations of 29 cross sections that are used to analyze the solutions. Both 2-D and 3-D simulations were conducted for this test case. Figure 7 shows the mesh generated on the bottom boundary over part of the domain containing the main stream. In the 3-D mesh, the horizontal resolution inside the main channel is around 1.25 m with a progressive coarsening to 20 m over the floodplain. The horizontal resolution is slightly lower inside the main channel in the 2-D simulation and similar to that used in the 3-D simulation over the floodplain. The higher resolution inside and around the main channel in the 3-D mesh was needed to avoid the development of spurious oscillations in the 3-D solution. The 3-D mesh was additionally refined in the vertical direction to resolve the bottom boundary layer and the flow features over the large-scale features of the bottom surface. The refinement procedure uses a trimmer cell procedure and prisms layers, as illustrated in Fig. 8.

The extent of the computational domain in the 2-D simulation was the same as the one used in the 3-D simulation. The 2-D model (Lai, 2008) was calibrated for both low and high flow conditions in the Iowa River. The outlet boundary condition in the 2-D model is based on a specified rating curve at the outlet boundary based on the available rating curve at Section 4-

4 in Fig. 6. In the 3-D simulation, the solution was simply extrapolated at the outlet boundary. The biggest difference between the two models is the geometry near the river dams. The 3-D model takes into account the exact shape of the dams based on old construction blueprints, while the 2-D model accounts for the presence of the dams by including a bump in the geometry with the same crest elevation as that of the constructed river dams.

During the June-July 2008 time frame, the Iowa River experienced the biggest flood in its history causing significant damage to several cities, including Iowa City. In the days before the flood event, the flow in the Iowa River reach analyzed here was quasi-steady (low flow conditions). Once the flooding event started, the discharge in the Iowa River was characterized by large temporal variations. The first three days of the flooding event will be analyzed. The hydrographs of three gaging stations located near the inlet section, right downstream of the 2nd river dam and in the Clear Creek stream are shown in Fig. 9b. One hydrograph corresponds to the USGS gaging station located 100 m downstream of the 2nd river dam. The other two gaging stations were used to specify the inlet boundary conditions for the Iowa River and Clear Creek. A first simulation was done corresponding to (steady) low flow conditions (time 0 in Fig. 9b), for which the river discharge was Q=245 m^3/s. The Froude number and the Reynolds number defined with the mean velocity (U=0.51 m/s) and mean water depth at the inlet section (H=5.45 m) were 0.07 and 2.8×10^6, respectively. The time step was 0.5 s. The total number of grid cells was close to 12 million in the 3-D and 0.7 million in the 2-D simulations. As shown in Fig. 9b, the 3-D model accurately predicts the temporal variation of the flowrate at the location of the USGS gaging station. The times to peak for the two relative maxima flowrates present in the hydrograph during the simulated time are accurately captured.

Figure 9a shows the free-surface elevation along the centerline of the channel predicted by the two models at (steady) low flow conditions, as well as field data measurements. Between the inlet boundary and the 1st river dam, the 2-D model underestimates the free-surface elevation with respect to field data, whereas the 3-D model follows very closely the field data, especially in regions close to the inlet. Around halfway in between the inlet boundary and the 1st river dam, the 3-D model starts to underestimate the elevation of the free surface. In between the 1st and the 2nd river dam, it is unclear which model represents the best the position of the free surface. Finally, downstream of the 2nd river dam, the 3-D model predictions are more accurate. The 2-D model consistently underestimates the free-surface elevation in the same region. In particular, the 3-D model successfully captures the changes in the free surface elevation around the two dams where the flow regime changes from subcritical to supercritical and then back to subcritical. No free surface measurements along the river reach were available once the flood event started. As the unsteady wave passes through the domain and the flowrates increase, the flow depths predicted by the 2-D model become eventually larger than the ones predicted by the 3-D model. At the end of the simulation time (Time 11 in Fig. 9b), the 2-D model is consistently overestimating the flow depths with respect to the 3-D model by 2-3%. While the differences between the flow depth predictions of two models at the latest time are relative low, the overall percentage change from Time 0 to Time 11 is relatively large, being as high as 10%.

While accurately predicting the location of the free surface is of most importance for flood modelling, an analysis of the velocity and unit-discharge distributions is also relevant. It was found that 22 out of the 29 cross sections showed very good agreement between the 3-D model and 2-D model unit-discharge profiles. Cross-sections 2, 8, 9, 11, 12, 13 and 14 showed relatively large differences. For example, Figs. 10a and 10b compare the unit-

discharge distributions at cross-sections 11 and 12 situated toward the exit from the high-curvature region (see Fig. 10c), where cross-stream secondary flow effects are expected to be significant. At both cross sections, the 2-D model predictions for low-flow conditions underestimate the redistribution of the streamwise momentum toward the outer bank. This is not surprising because this redistribution is driven by the formation of the cross-stream cells of secondary flow that cannot be captured by 2-D models. The differences between the low-flow unit-discharge predictions at Section 12 are even larger than those observed at Section 11. This is in part because two relatively deep scour holes are present in the channel between Sections 11 and 12 (Fig. 10c).

When comparing the unit-discharge profiles predicted by the two models during the flooding event, it was found that cross sections that showed good agreement at low-flow conditions also showed relatively good agreement throughout the duration of the simulation. However, at sections where the solutions showed significant differences at low-flow conditions (Time 0), the agreement worsened as the flood wave started propagating through the domain. This can be clearly shown in Figs. 10a and 10b that compare the unit discharge profiles at time 0 and time 8 for the 2-D and 3-D simulations. At all times, the 2-D model predicts a much more symmetric distribution of the unit discharge with respect to the centerline of the main channel compared to the 3-D model results. Moreover, at these sections, the 3-D model predicts that the region of high streamwise velocity moves toward the outer bank with increasing total discharge, an effect that the 2-D model cannot capture.

5. Flood wave propagation in a domain containing a 7-km long reach of the Iowa River

To investigate the efficiency of flood protection measures, a 7-km long Iowa River sub-reach of the 18-km long reach considered in the previous section was chosen to conduct a series of simulations. The 7-km long reach starts upstream of the 1st river dam and extends some distance downstream of the 2nd river dam (Fig. 11). As already mentioned, the dams are in fact weir structures. Figure 12 shows the bathymetry/topography inside the computational domain together with the location of the cross sections that will be used for a more detailed analysis of the solution, as well as the hydrograph that was specified at the inlet of the domain. The peak discharge was about 30% larger than the peak discharge during the 2008 flood, such that the efficiency of flood protection measures can be fully tested. In the 3-D simulations, the average grid resolution in the horizontal directions was 5 m in the main channel and 20 m over the floodplain. The 3-D mesh contained close to 10 million cells and the time step was 0.1 s. The 2-D model used a mesh with similar level of grid resolution in the horizontal directions. Steady-state conditions were simulated for a flowrate of approximately 1,150 m^3/s, which corresponds to flow conditions close to the peak flowrate experienced during the flood of 2008. Then, a sinusoidal unsteady wave with a flowrate amplitude of 600 m^3/s propagated into the domain. The 3-D model is also used to assess the effectiveness of deployment of temporary floodwalls in regions that are important to be protected against flooding. Most of the 3-D simulations were run on 64 processors (16 cores of 2.6GHz with 4 GB RAM/processor) of a PC-cluster with Myrinet inter connection. The 3-D simulations took about 150 hours to complete. By comparison, the calibrated 2-D model simulation was run on a single processor and took 16 hours to complete.

5.1. Comparison between the 3-D and 2-D model predictions for the base case

Figures 13b and 13c compare the flooding extent predicted by the 3-D and 2-D simulations at the initial steady state (time=0). Also shown in Fig. 13a is an aerial photograph taken after the

peak of the flood of 2008, at approximately the same discharge (Q=1,150 m^3/s) corresponding to the initial steady state. In Figs. 13b and 13c, the solid black line denoting the extent of the flooded region in the field was superimposed on the plots showing the flooded regions predicted by the 3-D and 2-D simulations, respectively. Overall, very good agreement is observed between the flooded regions predicted by the numerical simulations and those observed in the field. The 2-D model inundates slightly more than the 3-D model. For example, this happens between Section 1 and the 1st dam and between Section 2 and Section 3. Overall, the 2-D model overestimates the flood extent by approximately 7% compared to the 3-D model results.

At steady state, both the 3-D and 2-D simulations predict a free surface elevation value at the location of the USGS gage within 0.05 m of the value obtained using the USGS rating curve. The USGS gage is located downstream of the 2nd dam, close to section 12 in Fig. 13. Over the whole reach, the maximum difference between the free surface elevations predicted by the 3-D and 2-D simulations at the initial steady state is close 0.3 m. On average, the 2-D simulation predicts a higher free surface elevation compared to the 3-D simulation at time = 0 hr. During the propagation of the unsteady wave, the differences between the free surface elevations predicted by the 3-D and 2-D simulations become larger. At peak flood extent (time = 3.5 hr) the maximum difference is close to 0.7 m. The 3-D simulation predicts the size of the flooded region at time = 3.5 hr (Fig. 13d) to be about 9% larger than the one predicted by the 2-D simulation. Still, overall good qualitative agreement is observed between the 3-D and 2-D predictions of the flooded area at peak flood extent.

More insight into the differences between the two solutions can be obtained by comparing the unit discharge distributions at selected cross sections (Fig. 14). Out of the 12 cross sections

where the two solutions were compared, only 3 cross sections showed significant differences between the unit discharge distributions at the initial state and at peak flood extent. The first one is Section 1, which is situated in a region of high channel curvature right before the 1st dam. The second one is Section 11, which is located in a straight reach upstream of the 2nd river dam where, in principle, one should not expect large differences between the two solutions. A very shallow region is present on the East side of the cross section. The 3-D model predicts a unit discharge distribution skewed towards the west side of the channel. By contrast, the 2-D model predicts a fairly symmetric and close to uniform unit discharge distribution away from the two banks. These differences are observed at both the initial state and at peak flood extent. Section 12 is located downstream of the 2nd river dam, where the flow is influenced by the hydraulic jump caused by the presence of the dam. Given that the flow is highly three dimensional around the hydraulic jump, the 3-D and 2-D solutions are very different from each other in this region. The 3-D model predicts a two-peak distribution of the unit discharge at Section 12 due to the way the plunging core of high velocities interacts with the bathymetry downstream of the dam, whereas the 2-D model predicts a fairly uniform unit discharge distribution. Overall, the differences between the distributions of the unit discharge in the selected cross sections at the initial steady state and those after the flooding wave enters the domain are comparable. Most of these differences occur in regions where 3-D effects are generated by large-scale bathymetry features, the presence of hydraulic structures or of high-curvature regions (see also Horna-Munoz and Constantinescu, 2016).

5.2. Use of floodwalls as a flood protection measure

Common flood protection strategies for regions surrounding a river include building levees, temporary flood protection walls, flood prevention dams and construction of ponds. In the case of the Iowa River near Iowa City, the favored approach of reducing the effect of floods

is the deployment of temporary floodwalls. Such floodwalls do not allow water to flow into certain areas but may severely constrict the available area for flow passage. The 3-D model is used to assess the effectiveness of installing floodwalls as a flood protection strategy. As summarized in Table 1, several regions where floodwalls may be installed (Scenario 1 to Scenario 4) are considered. Currently, Iowa City is ready to install temporary floodwalls that extend from halfway between Sections 8 and 9 until Section 12 once a large flood is forecast. These floodwalls are called FW3. Additional floodwalls are proposed to be installed to protect regions situated near Section 1 and the 1st Dam (FW 1), and between Section 3 and halfway between Sections 5 and 6 (FW 2).

Steady state and unsteady solutions were obtained for the same flow conditions considered for the base case (no floodwalls) in Section 5.1. Figure 15 shows the flooded region at peak flood extent for the cases where floodwalls were installed in the computational domain (case Scenario 1 to 4) and for the base case. Floodwalls FW 3 are shown in red, whereas FW 1 and FW 2 are shown in blue.

Table 1 Flood protection strategies based on the use of floodwalls and removal of dams

Scenario 1	FW 3
Scenario 2	FW 1 + FW 3
Scenario 3	FW 2 + FW 3
Scenario 4	FW 1 + FW 2 + FW 3
Scenario 5	Removal of 2nd dam
Scenario 6	Removal of both dams

Comparison of Figs. 15a and 15b shows that floodwalls FW 3 can protect areas in their close vicinity from flooding at peak flood extent without increasing in a significant way the

flooding area upstream of their location. A slight increase of the flood extent is observed between Section 1 and the 1st dam, as well as between Section 2 and Section 3 for case Scenario 1 compared to the base case. The slight increase of the flood extent in the aforementioned regions is overshadowed by the large reduction of the flood extent in the vicinity of FW 3. The net flood extent reduction is approximately 8% at the initial steady state and at peak flood extent for case Scenario 1 compared to the base case. Case Scenario 2 can efficiently protect against flooding regions situated in between Sections 1 and 2 at peak flood extent (Fig. 15c). These areas are flooded in the base case and in case Scenario 1. Protecting this region is important, as several hospitals are located there. At all times during the propagation of the flood wave, the flood extent reduction is 18-19% in case Scenario 2 compared to the base case. Case Scenario 3 (Fig. 15d) significantly reduces flooding between Section 3 and Section 6, at both the initial steady state and at peak flood extent. A major residential area is located in the neighborhood of Sections 3 to 6. The flood extent reduction for case Scenario 3 is approximately 15% at the initial steady state and 14% at peak flood extent compared to the base case. Case Scenario 4 includes all floodwalls deployed in the previous cases (Fig. 15d). As expected, the regions situated in the neighborhoods of Sections 1 and 2 and of Sections 3 to 6 are well protected at peak flood conditions. The predicted reduction of the flooded area is 25% at the initial steady state and 26% at peak flood extent compared to the base case. Thus, for case Scenarios 1 to 4 the reduction of the flood extent is about the same for both the initial steady state and at peak flood extent conditions. Moreover, even for case Scenario 4 that contains the largest number of floodwalls, no significant flooding is predicted in regions situated away from the floodwalls compared to the base case.

The presence of the floodwalls modifies the unit discharge distribution in their vicinity with respect to the base case. This is always the case in cross sections cutting through the

floodwalls. The overall effect is an increase of the mean velocity in the cross section with respect to the base case. This is illustrated in Fig. 16 which compares the unit discharge distributions at Section 5. The largest differences are observed for case Scenarios 3 and 4 that contain the FW2 floodwall at the left bank. Figures 16b and 16c show how the streamwise velocity distribution change in the cross section as a result of the presence of the FW2 floodwall in case Scenario 4 compared to the base case. In particular, the core of large streamwise velocities is pushed toward the right bank. As the total cross-sectional discharge is not very different in the five cases analyzed here, the unit discharge values at a given time should be larger in between the extremity of the floodwall and the right bank for case Scenarios 3 and 4 compared to the other cases. This is confirmed by the unit discharge distributions in Fig. 16a that show that the peak unit discharge is about 10-15% larger in case Scenarios 3 and 4 compared to the base case.

Figure 17 shows the free-surface elevation profile along the centerline for the five cases. No significant differences are observed at both the initial steady state and at peak flood extent among the different simulations. Compared to the base case, the maximum increase of the free surface elevation for the cases with floodwalls is about 0.3 m and occurs at peak flow conditions when lots of the floodplain is inundated and thus a large increase in the flow discharge results in a relatively small increase in the free surface elevation. Overall, comparison of the simulations results in Figs. 15 and 17 shows that the proposed floodwall designs can effectively protect the critical regions situated in the vicinity of the Iowa River while not increasing significantly flooding away from these regions, with case Scenario 4 offering a comprehensive protection of the critical regions situated in the vicinity of the river reach.

6. Flood wave propagation in a domain containing a 2-km long reach of the Iowa River and a bridge deck that can become submerged at high flows

This section focuses on the simulation of a flood wave advancing in a 2-km long reach of the Iowa River near Iowa City. The computational domain and the bathymetry are visualized in Fig. 18a. The reach contains a river dam (same as 2nd river dam in Fig. 12a) and a bridge deck corresponding to a bridge situated in the immediate vicinity of the dam (Fig. 18b). The length, width and thickness of the bridge deck were 60 m, 20 m and 0.2 m respectively. The bridge deck was situated at about 4 m above the bottom of the main river channel at that location. The mesh was refined around the bridge deck and around the crest of the weir corresponding to the river dam (Fig. 18c) to resolve the flow structures generated by the interaction of the flow with the bridge deck and the river dam. The mesh resolution was consistent with the one of the test cases discussed in the previous two sections. The 3-D mesh contained close to 3 million cells. The time step was 0.1 s. A full unsteady solution took 70 hours to complete when run on 64 processors of the same PC cluster used to perform the other simulations in complex domains.

The inflow hydrograph (Fig. 18d) was chosen such that the bridge deck becomes submerged when the flood wave reaches the bridge and will remain so for several hours. As this happens, the flow regime changes from open channel flow to pressurized flow before changing back to open channel flow after the flood starts receding. Occurrence of pressurized flow over an erodible bed is known to generate larger bed shear stresses and thus severe scour. These effects are referred to as pressure scour effects. While all previous test cases can also be calculated using 2-D models, this is not the case for applications when the flow becomes pressurized around a hydraulic structure or a flow obstruction. Even non-hydrostatic 2-D models cannot be applied for such cases as the main modelling assumptions are violated. The

same is true for hydrostatic 3-D models. The only way to obtain meaningful information on flow hydrodynamics and the capacity of the flow to entrain sediment is via a fully 3-D non-hydrostatic model simulation. To better understand the flow modifications induced by the bridge deck once it becomes submerged, an additional simulation in which the bridge deck was not present was performed with identical boundary conditions and inflow hydrograph.

At times when the bridge deck is not submerged (e.g., before the flood wave arrives in the region where the bridge is situated), the streamwise velocity distribution in spanwise cross sections cutting through the bridge deck (e.g., at Section 1 in Fig. 18a) is qualitatively similar to that observed at cross sections situated upstream of the bridge deck (e.g., at Section 2 in Fig. 18a). The core of high streamwise velocities penetrates more on the deeper half of the main channel but does not move far away the center of the two cross sections (see Figs. 19a and 19c at time=0.3 hrs). As the region around the bridge starts being flooded and the bridge deck becomes submerged, the free surface elevation increases and the core of high streamwise velocities moves even more toward the deepest part of Section 2 (see Fig. 19b at time=2.0 hrs). The same is true for the region situated beneath the bridge deck where the flow becomes pressurized (Fig. 19d at time=2.0 hrs). Though the discharge in Section 1 in the pressurized flow region (1,350 m^3/s) is less than the one at Section 2 at the same time instant (1,640 m^3/s), the bed shear stresses are considerably larger in Section 1. This is because the core of high streamwise velocities moves closer to the bed at the cross sections where the flow is pressurized and also extends laterally significantly more toward the shallower side of the cross section (see Figs. 19b and 19d).

One should also mention that the occurrence of pressurized flow can also act toward decreasing the bed shear stress in regions situated upstream (e.g., due to backwater flow

effects induced by the bridge deck obstruction) or downstream of it. This is mostly because once the flow becomes pressurized, the submerged bridge deck changes the direction of the flow approaching the crest of the weir.

Figure 20 offers more quantitative evidence of the effects the change in the flow regime has on the bed shear stresses and, consequently, on the sediment entrainment capability of the flow beneath the bridge deck. To isolate pressurized flow effects, the temporal variation of the width-averaged bed shear stress in Section 1 (Fig. 18a) in the simulation containing the bridge deck is compared with results from a simulation containing no bridge deck where the flow regime remains the same (open channel flow) during the propagation of the hydrograph. As expected, the bed shear stresses are basically identical until the time when the flow becomes pressurized in the simulation containing the bridge deck. Interestingly, there are very little time history effects, such that once the free surface elevation decreases below that of the bridge deck, the bed shear stresses predicted in the two simulations are again close to identical. During the time the flow is pressurized, the increase in the bed shear stress is very significant (up to 50%) in Section 1. The predicted spatio-temporal distributions of the bed shear stress in the two simulations can be used to estimate sediment entrainment during the flood event in the region situated directly beneath the bridge deck (e.g., using Van Rijn formula, van Rijn, 1984). For the mean sediment size present in the main channel (d_{50}= 1 mm), the erosive capacity of the flow during the time interval when the flow is pressurized in the simulation with the bridge deck is close to two times larger than during the same time interval in the simulation without the bridge deck. As most of the sediment entrainment at bridge sites occurs at high flow conditions, being able to estimate the maximum sediment entrainment capacity of the flow during a flooding event is of great importance. For cases,

when the flow changes regime locally, such estimations can only be obtained using the type of numerical models used in this study.

7. Final discussion and conclusions

A 3-D, non-hydrostatic RANS model with deformable free-surface capabilities was developed within an existing CFD code to simulate flood propagation in natural river environments containing man-made structures. This is one of the first applications of time-accurate RANS for this type of problems. The 3-D model was first validated for several simpler cases that tested the different features of the model and in particular its ability to capture the free surface position for steady and unsteady problems. It was found that the 3-D model was able to accurately reproduce results obtained in laboratory experiments.

The model was then applied to calculate steady flow and flood wave propagation in domains containing a reach of the Iowa River of a length of up to 18 km. To better understand the performance of the 3-D model, simulations were also performed using a calibrated 2-D hydrostatic depth-averaged code that is routinely used to obtain flood predictions in the Iowa River. Not surprisingly, the largest differences between 3-D and 2-D model predictions for these cases were observed in regions where 3-D effects (e.g., strong secondary cross-stream currents, strong vertical nonuniformity of the flow) are expected to be important.

In the case of the 18-km long river reach test case with steady low-flow conditions, the 3-D model was able to predict the free-surface elevation more accurately compared to the 2-D model. When an unsteady hydrograph was propagated into the domain, the 3-D model was able to reproduce the hydrograph recorded by a gaging station located within the domain with small differences. During the simulated hydrograph, the differences between the 3-D and 2-D

predictions of the free surface elevation were as high as 10%. For the high-flow conditions present in the 7-km long river reach test case, the floodplain is flooded. This adds an additional challenge for numerical models, as 3-D effects can be relatively important at the interface between the main channel and its floodplains at certain times during the propagation of the flood wave. In terms of the surface flooded, the differences between the 2-D model and the 3-D model predictions were 7% and 9% at the initial steady state and at peak flood extent, respectively. The validated 3-D model was then used to test the effectiveness of placing flood-protection walls at different critical locations that need to be protected in the case of a flood event.

Finally, the 3-D model was used to predict interaction of a flood wave with a bridge deck that becomes submerged during the time the peak flow passes the region containing the bridge. Such type of applications, in which the flow regime changes locally from open channel flow to pressurized flow and back to open channel flow, cannot be correctly simulated even using state-of-the-art 2-D non-hydrostatic models because the main assumptions in these models are severely violated. For such applications, 3-D models are the only option to accurately predict the interaction of the flood wave with the hydraulic structure and its effect on flow hydrodynamics (e.g., backwater flow effects can be induced at large distances from the location where the flow becomes pressurized), bed friction velocity distributions and sediment entrainment potential. Though not considered in the present study, coupling of such a 3-D model with a morphodynamics model will allow studying pressure scour effects.

The main challenge of using 3-D models for routine predictions of flood propagation in natural systems is the associated computational cost and resources required to perform the simulations.

Not surprisingly, the computational resources and physical times needed to perform the 3-D simulations reported in the present study and to generate the data bases were much larger than those required by the 2-D simulations. With the rapid increase of computational power, access to large-scale computational resources needed to perform such 3-D simulations in a reasonable amount of time will continue to decrease fast, such that such computations will start being used to study real flood scenarios in diverse environments. One important point is that the present 3-D simulations in complex domains (natural bathymetry containing large-scale man-made structures) were run only on 64 processors. On the type of PC clusters used to perform the simulations reported in the present study, the numerical solver scales well up to about 1,000 processors so, if computational resources are widely available, the physical time needed to obtain a 3-D solution can be decreased by about one order on magnitude. This is an important point especially for flood problems that cannot be correctly predicted using lower-order models and for which 3-D non-hydrostatic models are the only option to numerically investigate the effects of flood wave propagation. Another important observation is that 3-D models that resolve most of the relevant bathymetry features requires, basically, no calibration. By contrast, the calibration step can be quite time consuming for lower-order models. For example, calibrating the 2-D model for the Iowa River region simulated in the various test cases discussed in the present study required several weeks.

Another main application of 3-D models of the type developed in the present study is for performing simulations of short flood events over relatively short domains containing hydraulic structures and other geometrical complexities where one suspects that the flow associated with the flood wave propagation will be subject to strong 3-D effects. A major problem with current application of 1-D and 2-D models to predict floods in complex domains is that one does not have good guidelines to know the range of problems that can be

accurately solved with such models and which geometrical and flow complexities result in a sudden decrease of the accuracy of their predictions. As shown by the present study, 3-D simulations of smaller-scale flood problems, though computationally expensive, are feasible. As such, they can be used as a numerical experiment based on which the predictive capabilities of lower order (e.g., 2-D hydrostatic, 2-D non-hydrostatic and 1-D) models can be better assessed and ideas to improve, or to better calibrate them can be tested. This is important, given that even laboratory experiments of flood wave propagation generally provide only a limited amount of data for validation. Data obtained from observations of floods occurring in real environments are even scarcer because of the hazard associated with collecting data during the floods (Molinari et al., 2017).

Acknowledgments

The authors would like to acknowledge the Iowa Flood Center for supporting this study. The authors would also like to acknowledge high-performance computing support (project DD-2015-GEO117) from the Oak Ridge Leadership Computing Facility (OLCF) and, in particular, Dr. J. Wells from the National Center for Computational Science at the Oak Ridge National Laboratory as well as from the High-Performance Computing Center at the University of Iowa. We would like to thank Prof. W. Krajewski and Prof. J. Odgaard for many insightful comments and for their support in completing this study.

References

Arico, C. and Re, C.L. (2016), "A non-hydrostatic pressure distribution solver for the nonlinear shallow water equations over irregular topography." *Advances in Water Resources*, 98, 47-69.

Basnet, K, Constantinescu, G., Muste, M. and Ho, H. (2015), "Method to assess efficiency and improve design of snow fences," *ASCE Journal of Engineering Mechanics*, 141(3), 04014136.

Bates, P.D., De Roo, A. P. J., (2000), "A simple raster-based model for flood inundation simulation," *Journal of Hydrology,* 236 (1-2), 54-57.

Biscarini, C., Di Francesco, S., and Manciola, P. (2010), "CFD modelling approach for dam break flow studies." *Hydrology and Earth System Sciences*, 14, 705-718.

Biscarini, C., Di Francesco, S., Rifoldi, E., and Manciola, P. (2016), "On The Simulation of Floods in a Narrow Bending Valley: The Malpasset Dam Break Case Study." *Water,* 8, 545-558.

Blanckaert, K. and de Vriend, H.J. (2010), "A nonlinear model without curvature restrictions for flow in open-channel flows." *J. Geophysical Research*, 115, f04011

Bristeau, M.O., Goutal, N. and Saint-Marie, J. (2011), "Numerical simulations of a non-hydrostatic shallow water model." *Computers and Fluids*, 47, 51-64.

Casas, A., Benito, G., Thorndycraft, V.R., and Rico, M. (2006), "The topographic data source of digital terrain models as a key element in the accuracy of hydraulic flood modelling." *Earth Surface Processes and Landforms*, 31, 444-456

Cheng, Z., Koken, M. and Constantinescu, G. (2018), "Approximate methodology to account for effects of coherent structures on sediment entrainment in RANS simulations with a movable bed and applications to pier scour," *Advances in Water Resources, ,* 120, 65-82, http://dx.doi.org/10.1016/j.advwatres.2017.05.019

CADAM 2000. Concerted action on dambreak modeling. *Final Report SR 571,* HR Wallingford UK.

Constantinescu, G.S. and Patel, V.C. (2000), "Role of turbulence model in prediction of pump-bay vortices," ASCE J. of Hydr. Engrg., 126(5), 387-392.

Dhondia, J. F., Stelling, G. S. (2002), "Application of One Dimensional-2 Dimensional Integrated Hydraulic Model for Flood Simulation and Damage Assessment," *Hydroinformatics, 1-12.*

Frank, E. A., Ostan, A., Coccato, M., and Stelling, G. S. (2001), "Use of an integrated one dimensional/two dimensional hydraulic modeling approach for flood hazard and risk mapping," In River Basin Management, by R. A. Falconer and W. R. Blain, 99-108. Southhampton, UK: WIT Press.

Gamry, H.K. and Steffler, P.M. (2005), "Two-dimensional depth-averaged modeling of flow in curved open channels," *J. Hydraulic Research,* 43(1), 44-55.

Haque, M.D., Constantinescu, G. and Weber, L. (2007), "Validation of a 3D RANS model to predict flow and stratification effects related to fish passage at hydropower dams," *J. Hydraulic Research*, 45(6): 787-796.

Horna-Munoz, D. and Constantinescu, G. (2016). "A critical assessment of the performance of standard 2D flood models based on results of 3D URANS simulations," *International Conference on Fluvial Hydraulics*, River Flow 2016, Saint Louis USA.

Hunter, N. M., Bates, P., Horrit, M., Wilson, M. (2007), "Simple spatially-distributed models for predicting flood inundation: A review," *Geomorphology*, 90, 208-225, https://doi.org/10.1016/j.geomorph.2006.10.021.

Kashyap, S., Constantinescu, G., Rennie, C., Post, G. and Townsend, R. (2012), "Influence of channel aspect ratio and curvature on flow, secondary circulation and bed shear stress in a bend," *ASCE Journal of Hydraulic Engineering*, 138(12), 1045-1059, DOI:10.1061/(ASCE)HY.1943-7900.000064.

Kelecey, F. J. and Pletcher, R. H. (1997), "The development of a free surface capturing approach for multidimensional free surface flows in closed containers*." Journal of Computational Physics,* 138, 939-980.

Keylock, C.J., Constantinescu, S. and Hardy, R.J. (2012), "The application of computational fluid dynamics to natural river channels: Eddy resolving versus mean flow approaches." *Geomorphology*, 179, 1-20, http://dx.doi.org/10.1016/j.geo-morph.2012.09.006.

Khosronejad, A., Le, T., DeWall, P., Bartelt, N., Woldeamlak, S., Yang, X. and Sotiropoulos, F. (2016) "High-fidelity numerical modeling of the Upper Mississippi River under extreme flood condition," Advances in Water Resources, 98, 97-113.

Lai, Y.G. (2008), "SRH-2D version 2: Theory and user's manual," Sedimentation and River Hydraulics Group, Technical Service Center, Bureau of Reclamation, Denver.

Lai, Y.G. (2010), "Two-dimensional depth-averaged flow modeling with an unstructured hybrid mesh," *J. Hydraulic Engineering*, 136(1), 12-23.

Lu, X., Dong, B. and Zhang, X. (2015), "A two-dimensional depth-integrated non-hydrostatic numerical model for nearshore wave propagation." *Ocean Modelling*, 96, 187-202.

Martin, J. C. and Moyce, W. J. (1952) "An experimental study of the collapse of liquid columns on a rigid horizontal plate." *Philosophical Transactions of the Royal Society of London. Series A, Mathematical and Physical Sciences*, 244, 312-324.

Milly, P. C. D., Wetherald, R. T., Dunne, K. A., Delworth, T. L. (2002), "Increasing risk of great floods in a changing climate change." *Nature, 415* (6871), 514-517.

Mohammed, T.A., Said, S., Baradie, M.Z., and Basri, S. (2006). "One Dimensional simulation of Flood Levels in a Tropical River System Using HEC-2 Model," *Proceedings of the Joint International Conference on Computing and Decision Making in Civil Engineering*. Montreal, Canada.

Molinari, D., Menoni, S. and Ballio, F. (2017). "Flood damage survey and assessment: New insight from research and practice," American Geophysical Union, 288 pages.

Mossa, M. (2007). "The floods in Bari: What history should have taught," *J. Hydraulic Research*, 45(5), 579-594.

Musser, J.W. and Dryer, T.R. (2005), "Two-dimensional Flood-Inundation Model for the Flint River at Albany, Georgia," *Proceedings of the 2005 Georgia Water Resources Conference*, April 25-27, 2005: University of Georgia, Athens, Georgia.

Olsen, N. and Stokseth, S. (2010), "Theree dimensional numerical modeling of water flow in a river with large bed roughness," *J. Hydraulic Research*, 33(4), 571-581.

Omer, C.R., Nelson, E.J., and Zundel, A.K. (2003), "Impact of varied data resolution on hydraulic modeling and floodplain delineation." *J. American Water Resources Association*, 39, 467-475.

Ottevanger, W. (2013) "Modeling and parametrizing the hydro- and morphodynamics of curved open channels," PhD Thesis, Delft University of Technology, Delft, The Netherlands.

Radice, A., Rosatti, G., Ballio, F., Franzetti, S., Mauri, M., Spagnolatti, M., and Garegnani, G. (2012) "Management of flood hazard via hydro-morphological river modelling. The case of the Mallero in Italian Alps," J. Flood Risk Management, online first, doi:10.1111/j.1753-318X.2012.01170.x, 2012

Rodi, W. (1984), "Turbulence models and their application in hydraulics," IAHR Monography

Rodi, W, Constantinescu, G. and Stoesser, T. (2013), "Large Eddy Simulation in hydraulics," IAHR Monograph, CRC Press, Taylor & Francis Group (ISBN-10: 1138000247) 310 pages

Soares-Frazao, S. (2002), "Dam-break induced flows in complex topographies. Theoretical, numerical and experimental approaches," PhD. Thesis, Louvain-la-Neuve: Universite Catholique de Louvain. Civil Engineering Department, Hydraulics Division.

Soares-Frazao, S. and Zech, Y. (2002). "Dam Break in channels with 90° bend." *J. Hydraulic Engineering*, 128 (11), 956-968.

Van Rijn, L. C. (1984). "Sediment pick-up functions." *J. Hydraul. Engineering*, 110 (10), 1494–1503

Vasquez, J.A., Millar, R.G. and Steffler, P.M. (2011), "Vertically-averaged and moment model for meandering river morphology," *Canadian J. Civil Engrg*., 38, 921-931.

Wagner, C.R., Mueller, D.S., and USGS. (2001), "Calibration and Validation of a Two-Dimensional Hydrodynamic Model of the Ohio River, Jefferson County, Kentucky," *Water Resources Investigations Report 01-4091*.

Wilcox, D. C. (1998), "Turbulence Modeling for CFD," Second edition. Anaheim: DCW Industries, 174 pages.

Yang, C., Lin, B., Jiang, C. and Liu, Y. (2010). "Predicting near-field dam-break flow and impact force using a 3D model," *J. Hydraulic Research*, 48 (6), 784-792.

Yen, C. L. (1967). "Bed configuration and characteristics of subcritical flow in a meandering channel," PhD. Thesis, The University of Iowa, Iowa City, Iowa.

Zeng, J., Constantinescu, G., Blanckaert, K. and Weber, L. (2008a), "Flow and bathymetry in sharp open-channel bends: Experiments and predictions," *Water Resources Research*, 44, W09401, doi:10.1029/2007WR006303.

Zeng, J., Constantinescu, S.G. and Weber, L. (2008b), "A 3D non-hydrostatic model to predict flow and sediment transport in loose-bed channel bends," *IAHR J. of Hydraulic Research*, 46(3), 356-372, 10.3826/jhr.2008.3328.

Zeng, J., Constantinescu, G. and Weber, L. (2010), "3D calculations of equilibrium conditions in loose-bed open channels with significant suspended sediment load," *Journal of Hydraulic Engineering*, 136(9), 557-571, DOI:10.1061/(ASCE)HY.1943-7900.0000213

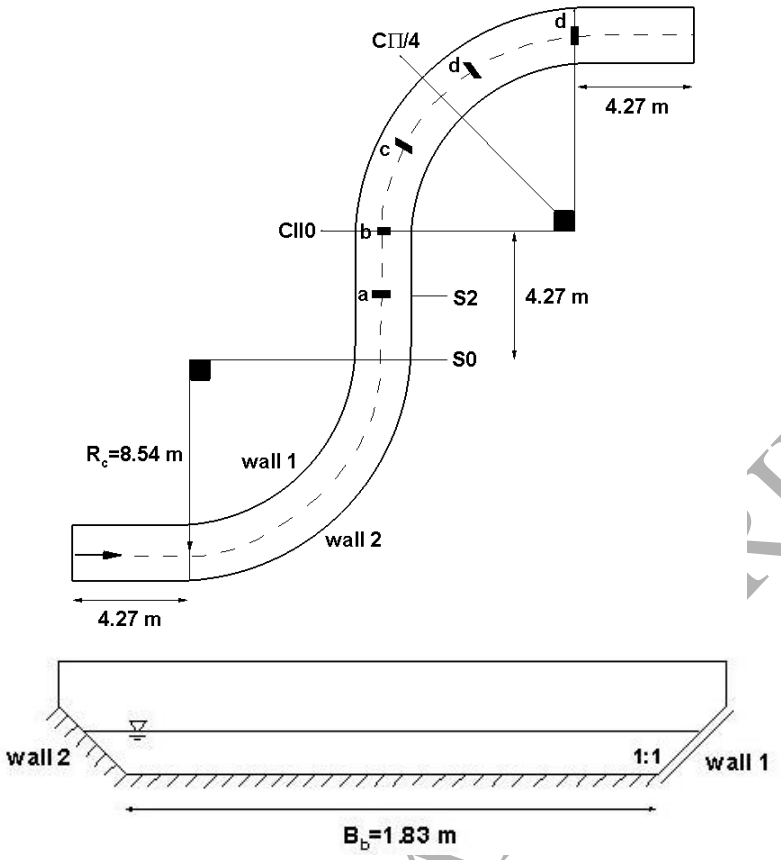

Figure 1. General experimental layout of the S-shaped channel experiment.

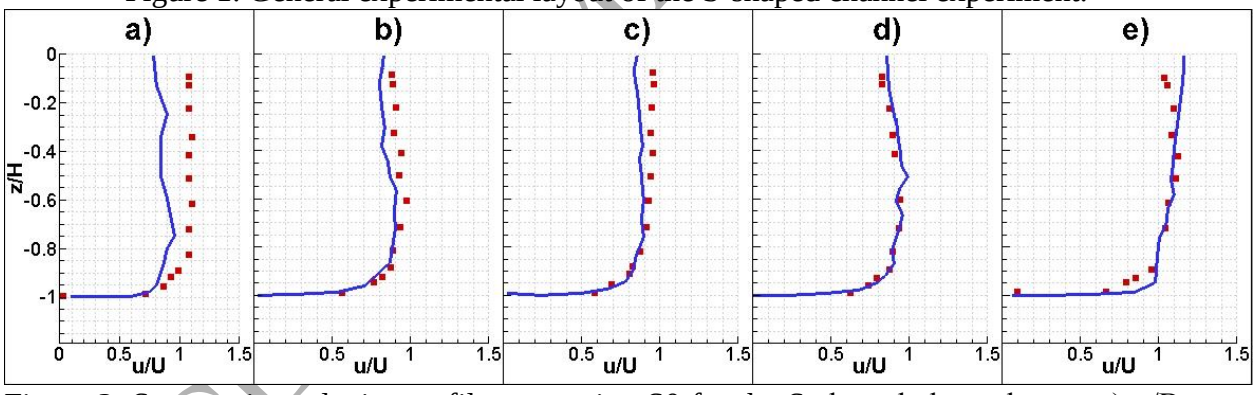

Figure 2. Streamwise velocity profiles at section S0 for the S-shaped channel case. a) η/B=-0.461; b) η/B=-0.307; c) η/B=0.0; d) η/B=0.307; e) η/B=0.461. The squares show the experimental data of Yen (1967) while the solid lines show the numerical simulation results.

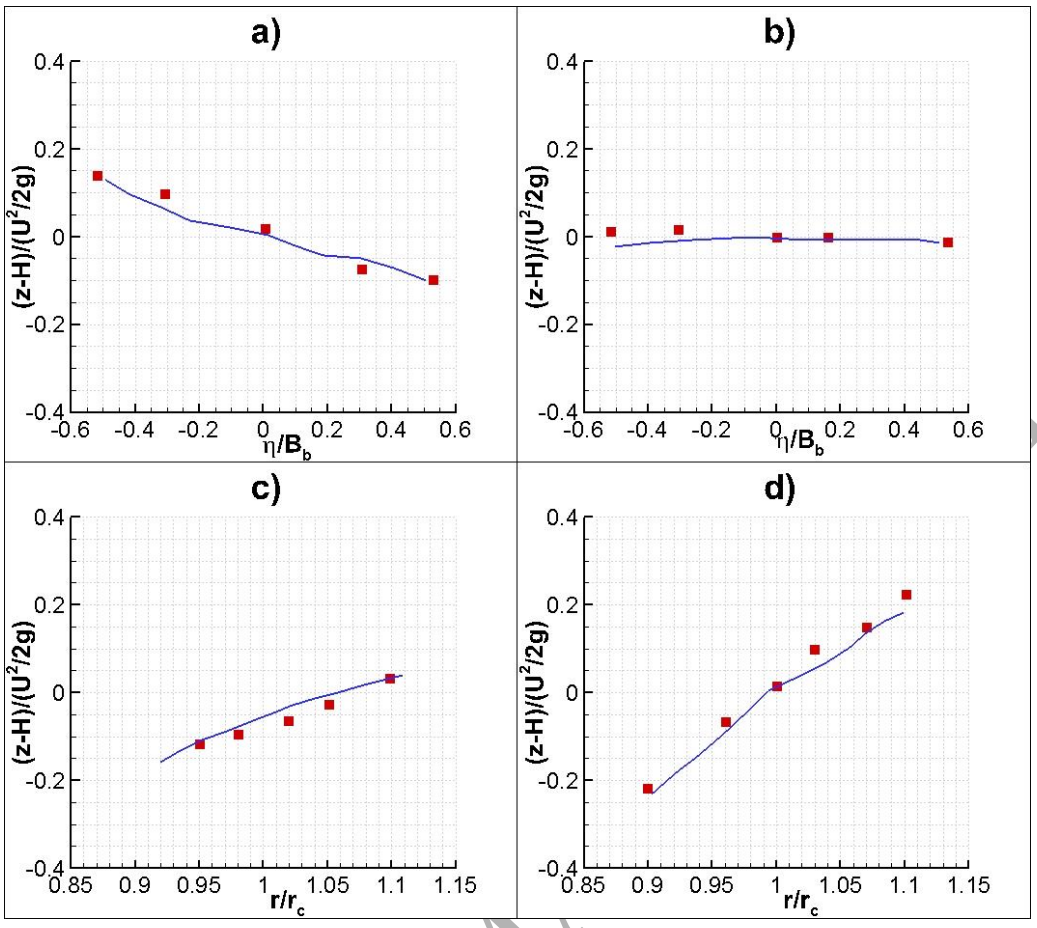

Figure 3. Transverse free-surface profiles for the S-shaped channel case. a) Section S0; b) Section S2; c) Section CII0; d) Section π/4. The squares show the experimental data of Yen (1967) while the solid lines show the numerical simulation results. The transverse variation of the free surface elevation is plotted as a function of η/B_b for the sections situated in the straight reach and as a function of the nondimensional radial distance r/R_c for the sections situated in the downstream curved reach.

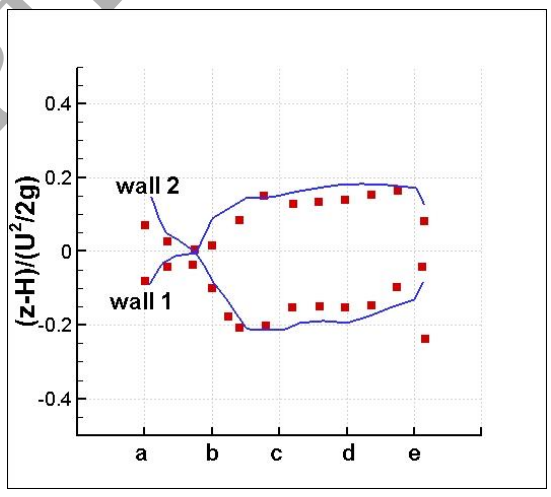

Figure 4. Longitudinal free-surface profiles near the two channel banks for the S-shaped channel case. The squares show the experimental data of Yen (1967) while the solid lines show the numerical simulation results. The positions of cross sections a to e are shown in Fig. 1.

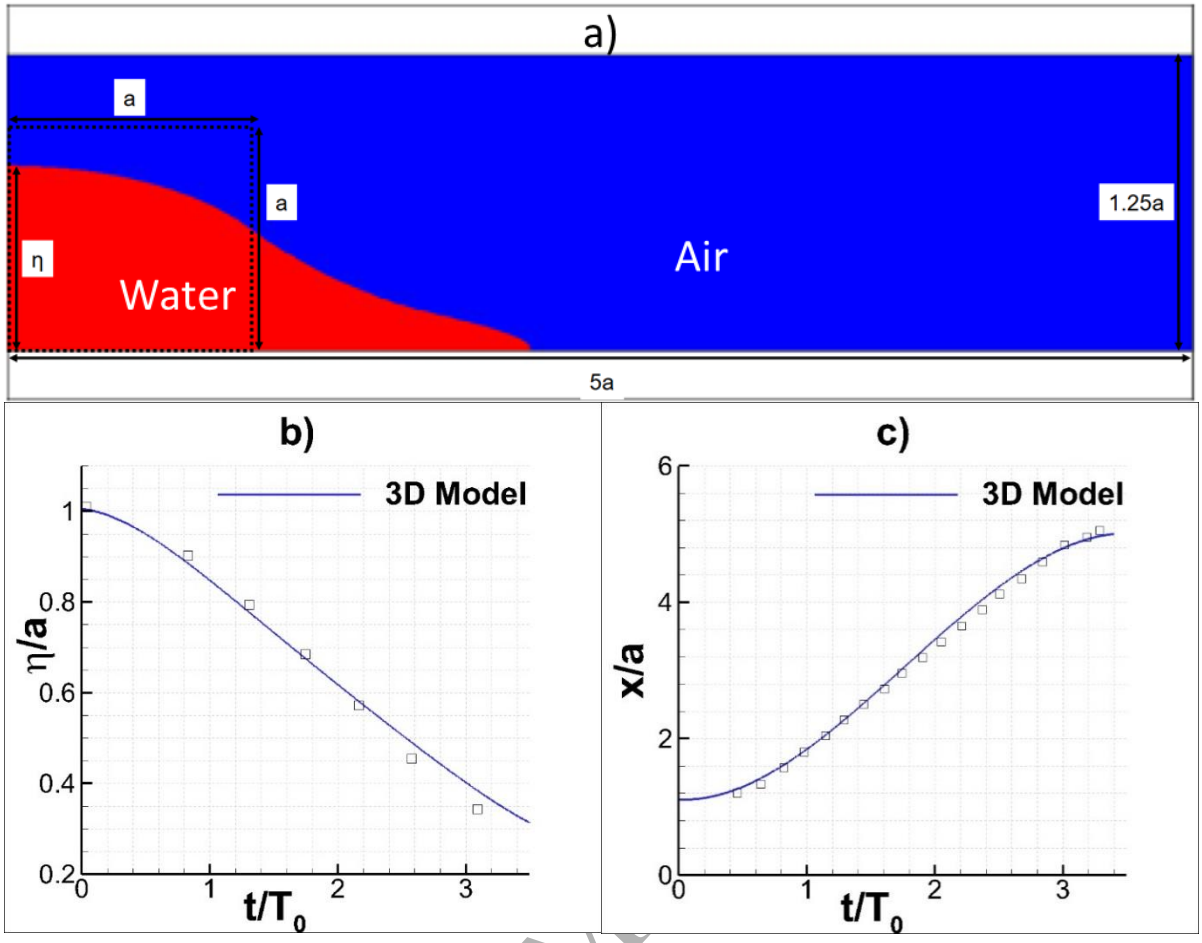

Figure 5. 2-D dam break case validation. a) Domain used in the simulation. The dashed square rectangle corresponds to the initial position of the region containing water; b) Water column height at the left wall vs. non-dimensional time; c) Front surge position measured from left wall vs. non-dimensional time. The squares show the experimental data of Martin and Moyce (1962), while the solid lines show the numerical results.

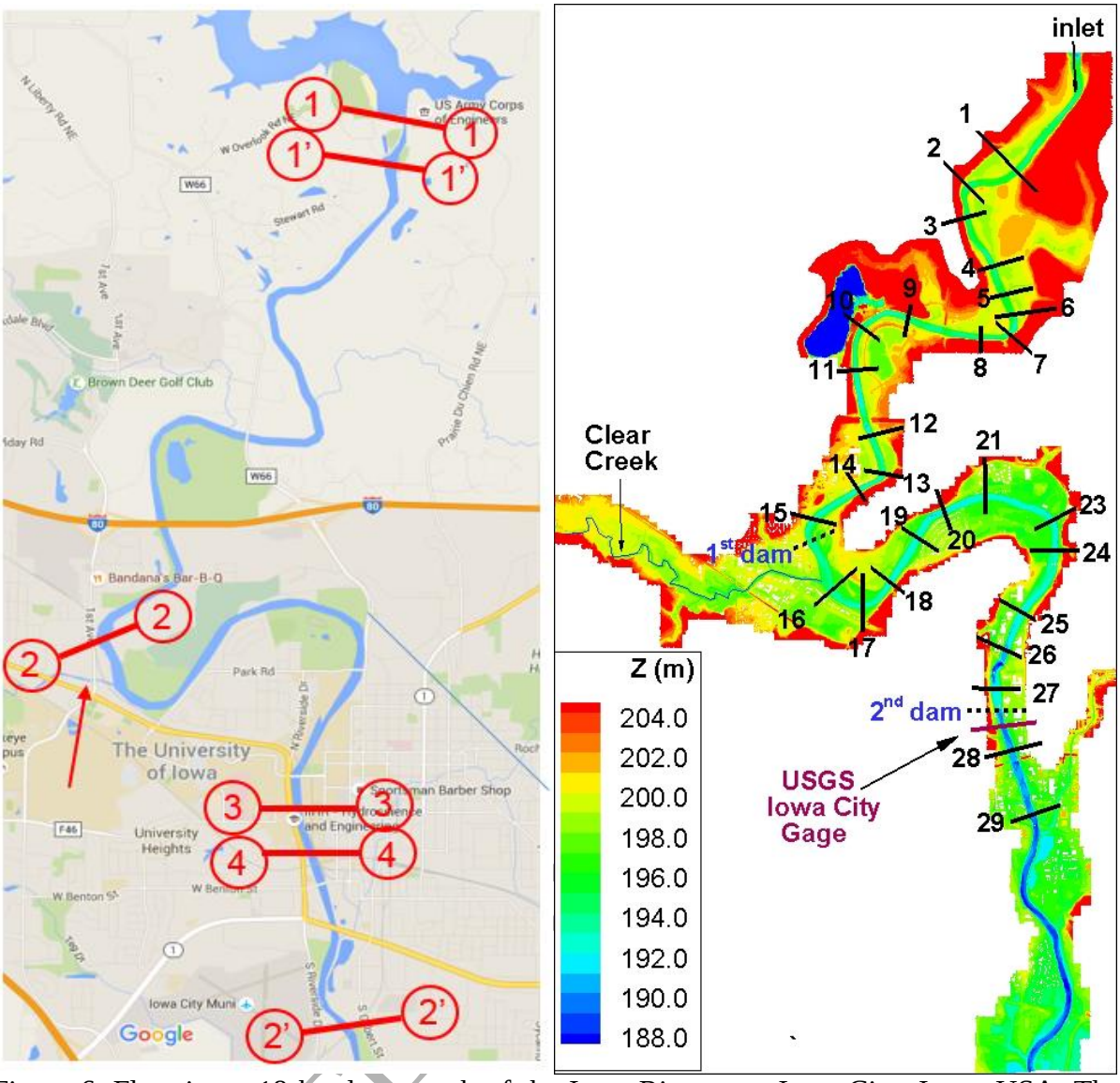

Figure 6. Flow in an 18-km long reach of the Iowa River near Iowa City, Iowa, USA. The locations of the flood control dam (1-1), the 1st river dam (2-2), the 2nd river dam (3-3) and the USGS gage (4-4) are indicated. The start and end of the computational domain correspond to sections (1'-1') and (2'-2'), respectively. The arrow points to Clear Creek, the main tributary of the Iowa River near Iowa City. The right frame shows the bathymetry/topography for the 18-km river reach simulation. The locations of the 29 cross sections, the two river dams and the main tributary (Clear Creek) are also shown.

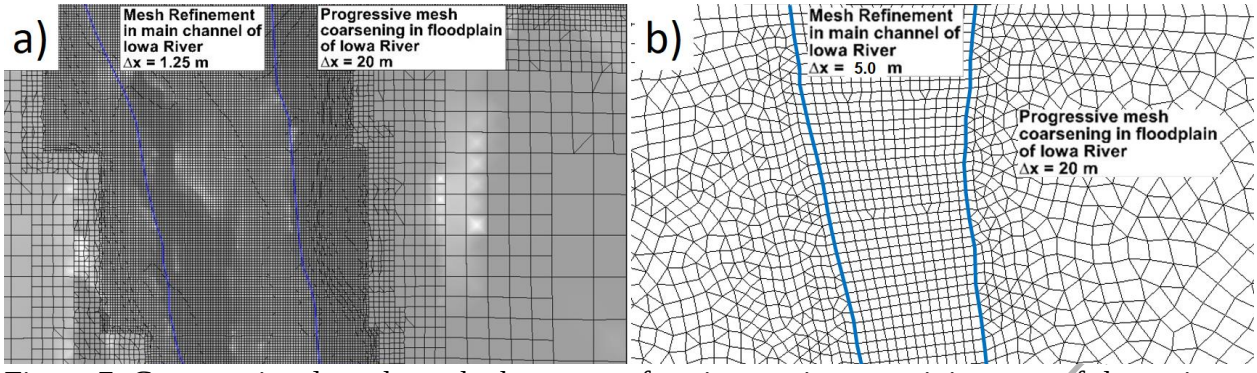

Figure 7. Computational mesh on the bottom surface in a region containing part of the main channel and its neighboring floodplain regions. a) 3-D model; b) 2-D model.

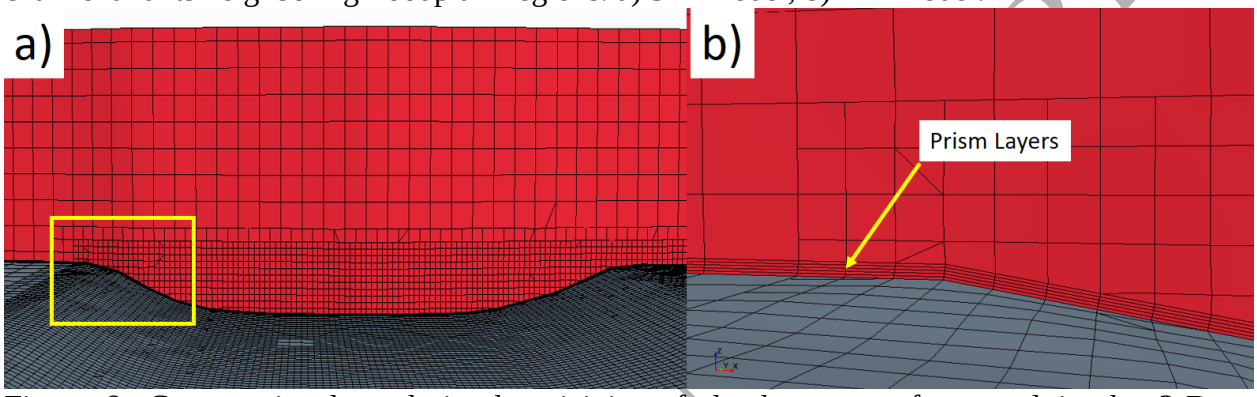

Figure 8. Computational mesh in the vicinity of the bottom surface used in the 3-D simulations. The mesh is refined near the bottom surface to resolve the boundary layer in the RANS simulation. a) mesh on the bottom surface and in a vertical plane; b) detail view of the mesh in the region corresponding to the rectangle shown in frame a.

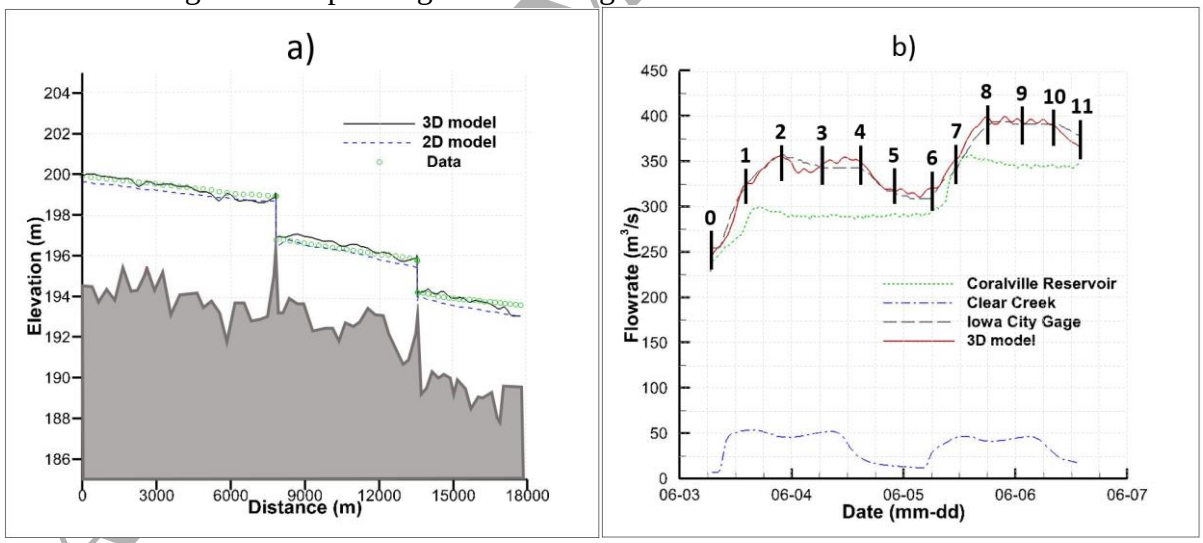

Figure 9. Flow in an 18-km long reach of the Iowa River. a) Free-surface elevation comparison between the 3-D model predictions, the 2-D model predictions and field data (symbols) at initial (low flow) conditions; b) Hydrograph predictions by the 3-D model for the flooding event occurring from June 3rd, 2008 until June 6th, 2008. Predictions are compared with measured flow rates at the Iowa City Gage. Specific times for further analysis are specified as vertical lines labelled 0 through 11.

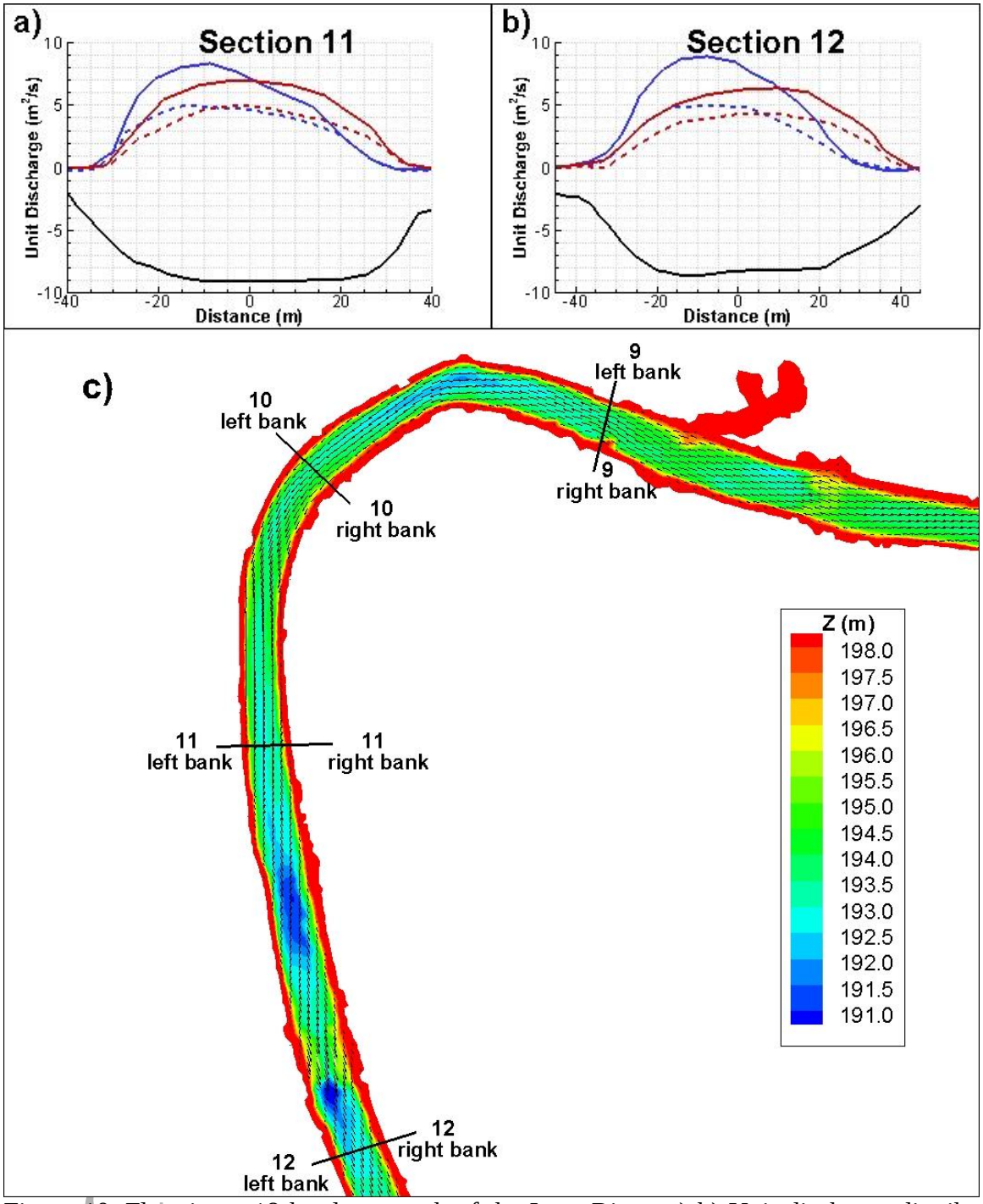

Figure 10. Flow in an 18-km long reach of the Iowa River. a)-b) Unit-discharge distribution comparison between 3-D (blue lines) and 2-D (red lines) simulation results at initial (low flow) conditions (dashed lines) and at Time 8 (solid lines); c) Free-surface velocity vectors near Sections 9 to 12 (3-D solution). The black line in frames a and b shows the bathymetry.

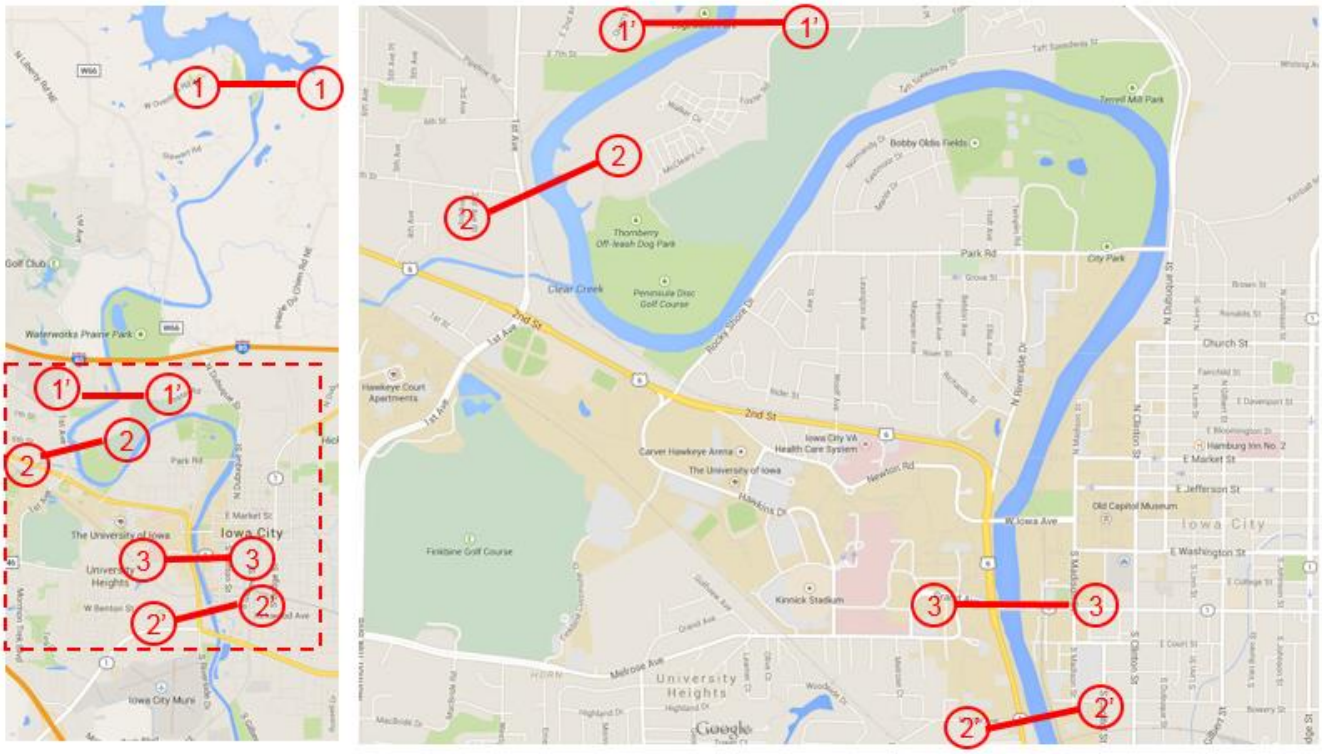

Figure 11. Flow in a 7-km long reach of the Iowa River near Iowa City, Iowa, USA. The locations of the flood control dam (1-1), the 1st river dam (2-2) and the 2nd river dam (3-3) are indicated. The start and end of the computational domain correspond to sections (1'-1') and (2'-2'), respectively. The right frame shows a close-up view of the computational domain.

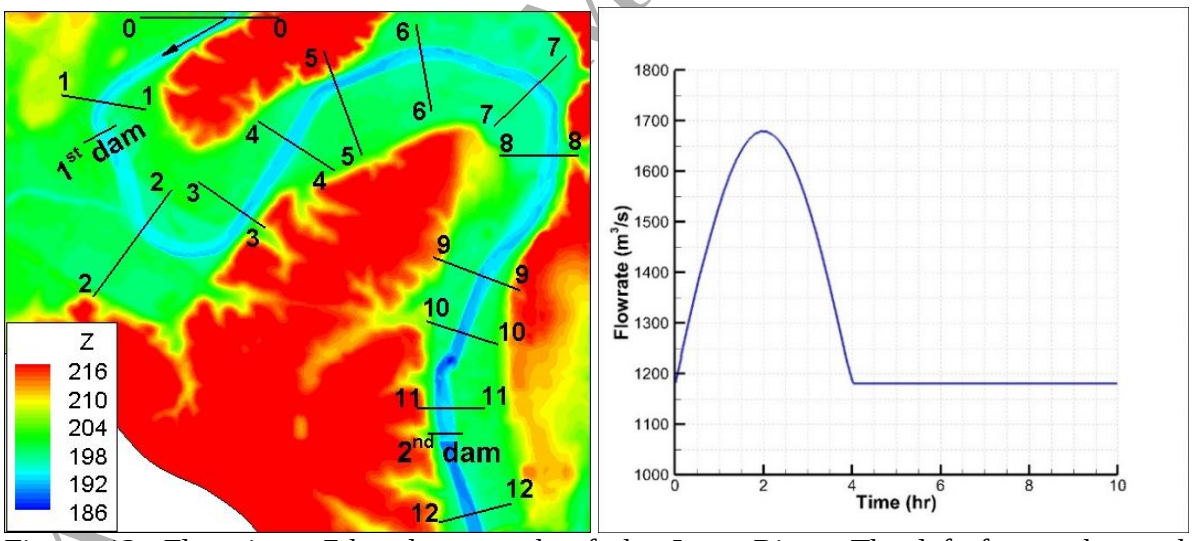

Figure 12. Flow in a 7-km long reach of the Iowa River. The left frame shows the bathymetry/topography used in the 3-D simulations with the locations of the 12 specified cross-sections. The right frame shows the sinusoidal hydrograph propagated into the reach. The hydrograph is introduced at section 0-0.

Figure 13. Flow in a 7-km long reach of the Iowa River. a) Aerial photograph of flooded region at a flowrate equal to that specified at steady state conditions; b) 3-D model prediction of flooded region at the initial steady state (time=0 hr); c) 2-D model prediction of flooded region at peak flood extent; d) 3-D model prediction of flooded region at peak flood extent. The buildings are also unsubmerged in the 3-D simulations but the isosurface showing the flooded region covers the buildings.

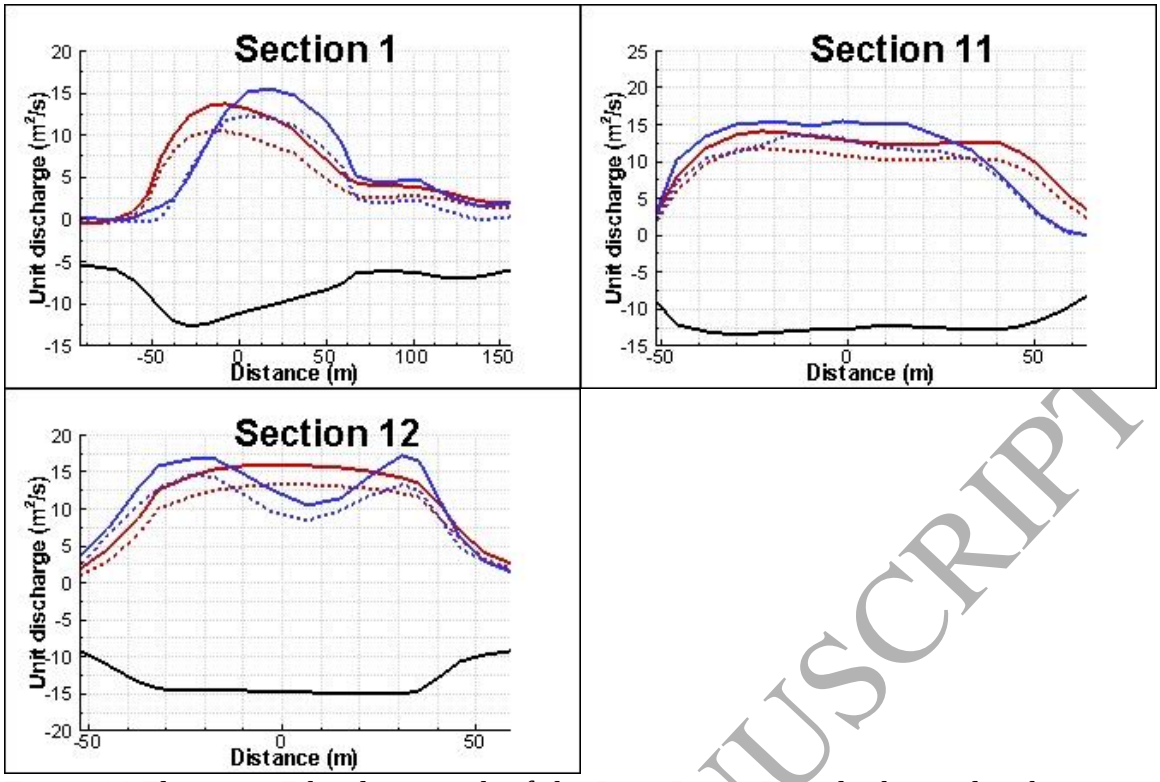

Figure 14 Flow in a 7-km long reach of the Iowa River. Unit discharge distributions at the initial steady state (dashed lines) and at peak flood extent (solid lines). Results are shown at three cross sections that showed significant differences between the 3-D (blue lines) and the 2-D (red lines) predictions. The black line shows the bathymetry.

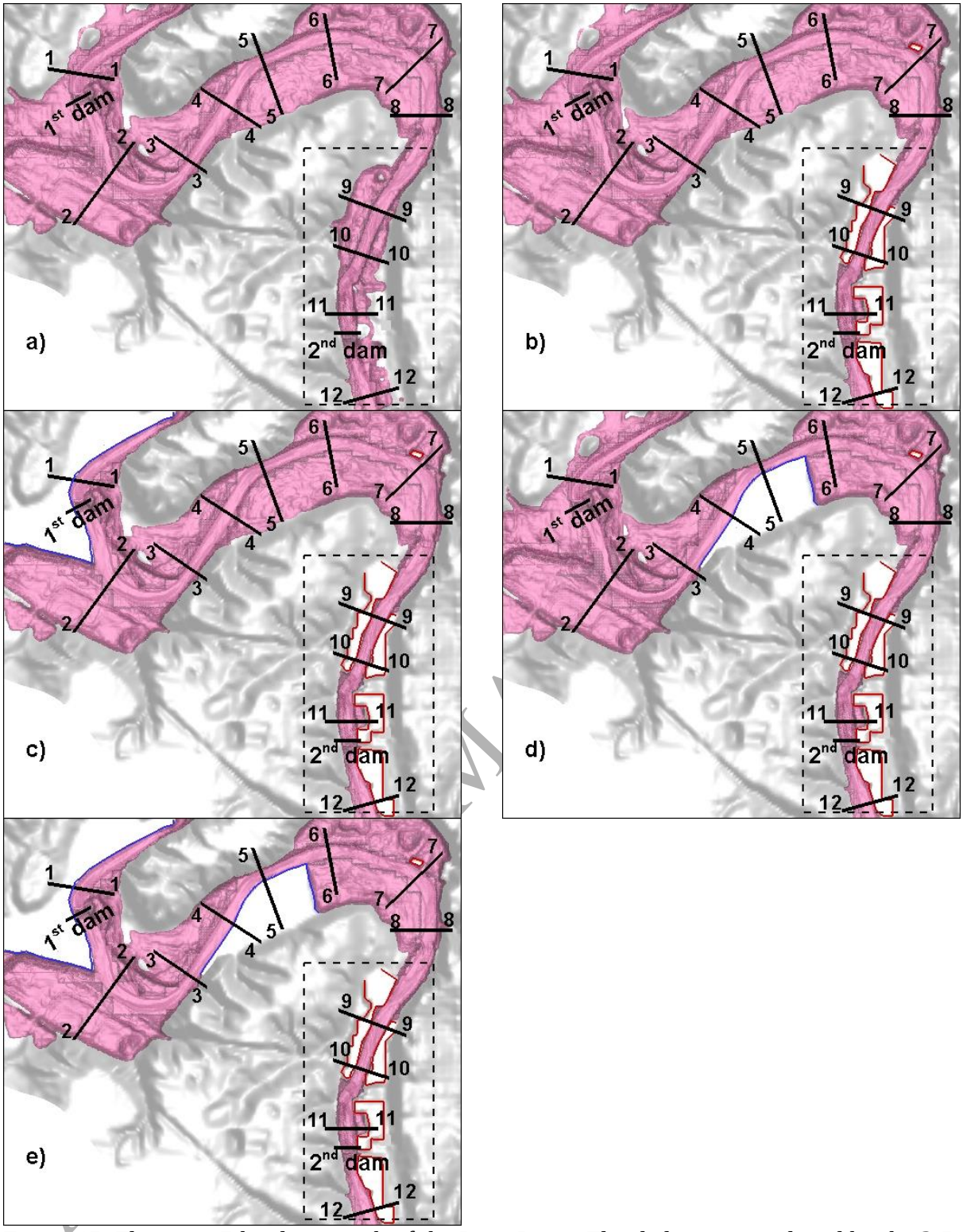

Figure 15. Flow in a 7-km long reach of the Iowa River. Flooded region predicted by the 3-D model at peak flood extent. a) base case; b) case Scenario 1; c) case Scenario 2; d) case Scenario 3; e) case Scenario 4.

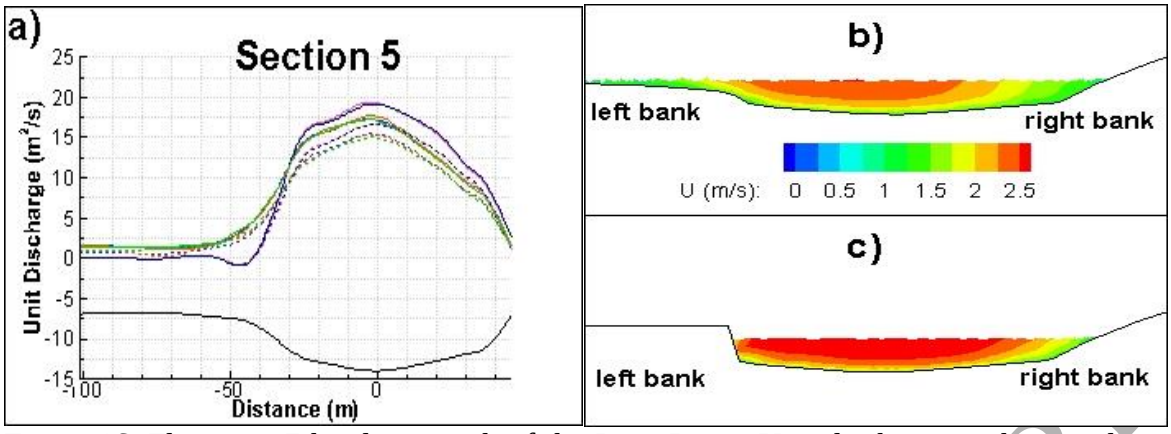

Figure 16. Flow in a 7-km long reach of the Iowa River. Unit discharge at the initial steady state (dashed lines) and at peak flood extent (solid lines). Results are shown at cross section 5 for the base case (blue lines) and for the cases containing floodwalls: case Scenario 1 (green lines), case Scenario 2 (orange lines), case Scenario 3 (pink lines) and case Scenario 4 (dark blue lines). Frames b and c show the streamwise velocity distribution at Section 5 at the initial steady state for the base case and for case Scenario 4, respectively. The black line in frame a shows the bathymetry.

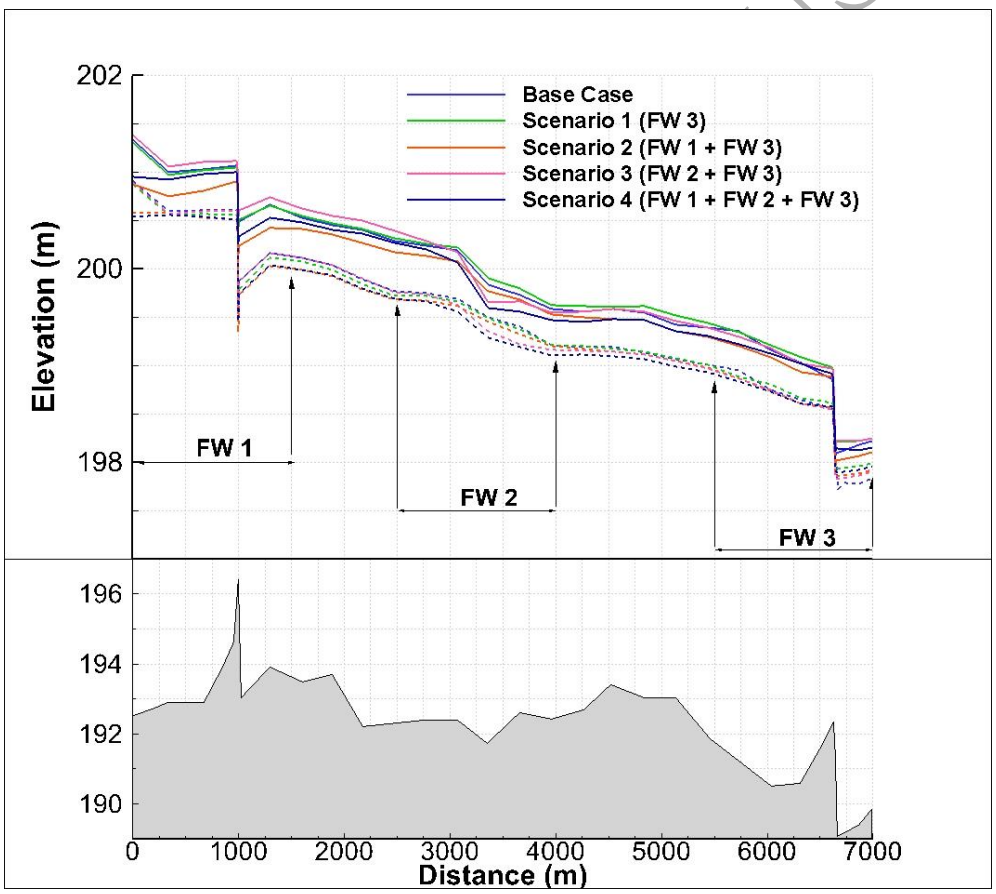

Figure 17. Flow in a 7-km long reach of the Iowa River. Free-surface elevation at the initial steady state (dashed lines) and at peak flood extent (solid lines). Base case (blue lines) results and compared with those of several cases containing floodwalls: case Scenario 1 (green lines), case Scenario 2 (orange lines), case Scenario 3 (pink lines) and case Scenario 4 (dark blue lines). The bottom part shows the bathymetry along the centerline.

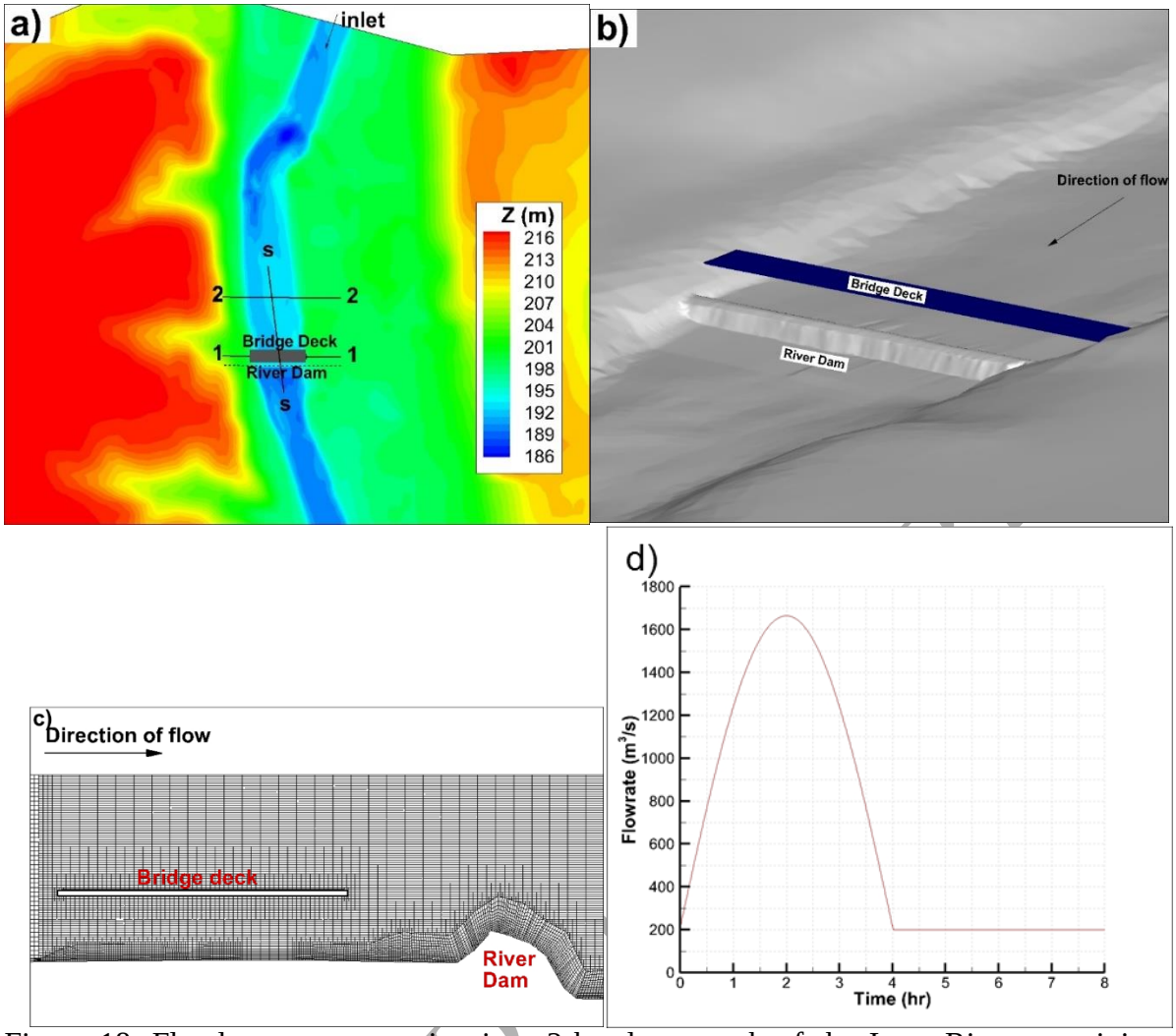

Figure 18. Flood wave propagation in a 2-km long reach of the Iowa River containing a bridge whose deck becomes submerged during the flooding event. a) aerial view with contour map showing bathymetry elevation; b) detail view of bathymetry close to the river dam (weir structure) and the bridge deck; c) mesh in a vertical plane cutting through the bridge deck and the dam, see section s-s in frame a; d) inflow hydrograph.

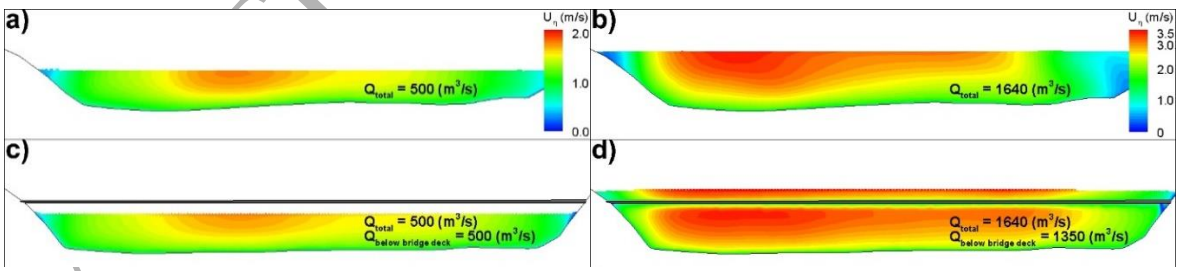

Figure 19. Streamwise velocity distributions at Sections 1, 2. The positions of the three sections are shown in Fig. 18a. Frames a and c show the streamwise velocity at Sections 2 and 1 at time = 0.3 hrs, before the bridge deck becomes submerged. Frames b and d show the streamwise velocity at the same sections at time = 2.0 hrs, after the bridge deck becomes submerged. The thin gray rectangle corresponds to the bridge deck.

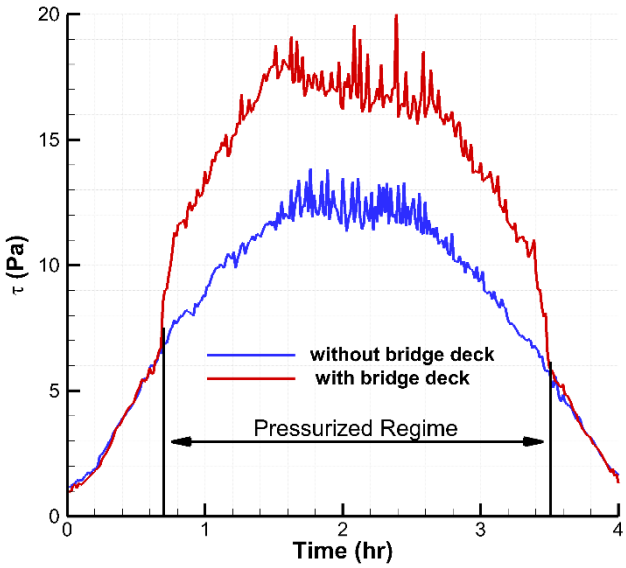

Figure 20. Temporal variations of the width-averaged bed shear stress at Section 1 predicted by the 3-D model. a) simulation with the bridge deck; b) simulation without the bridge deck.